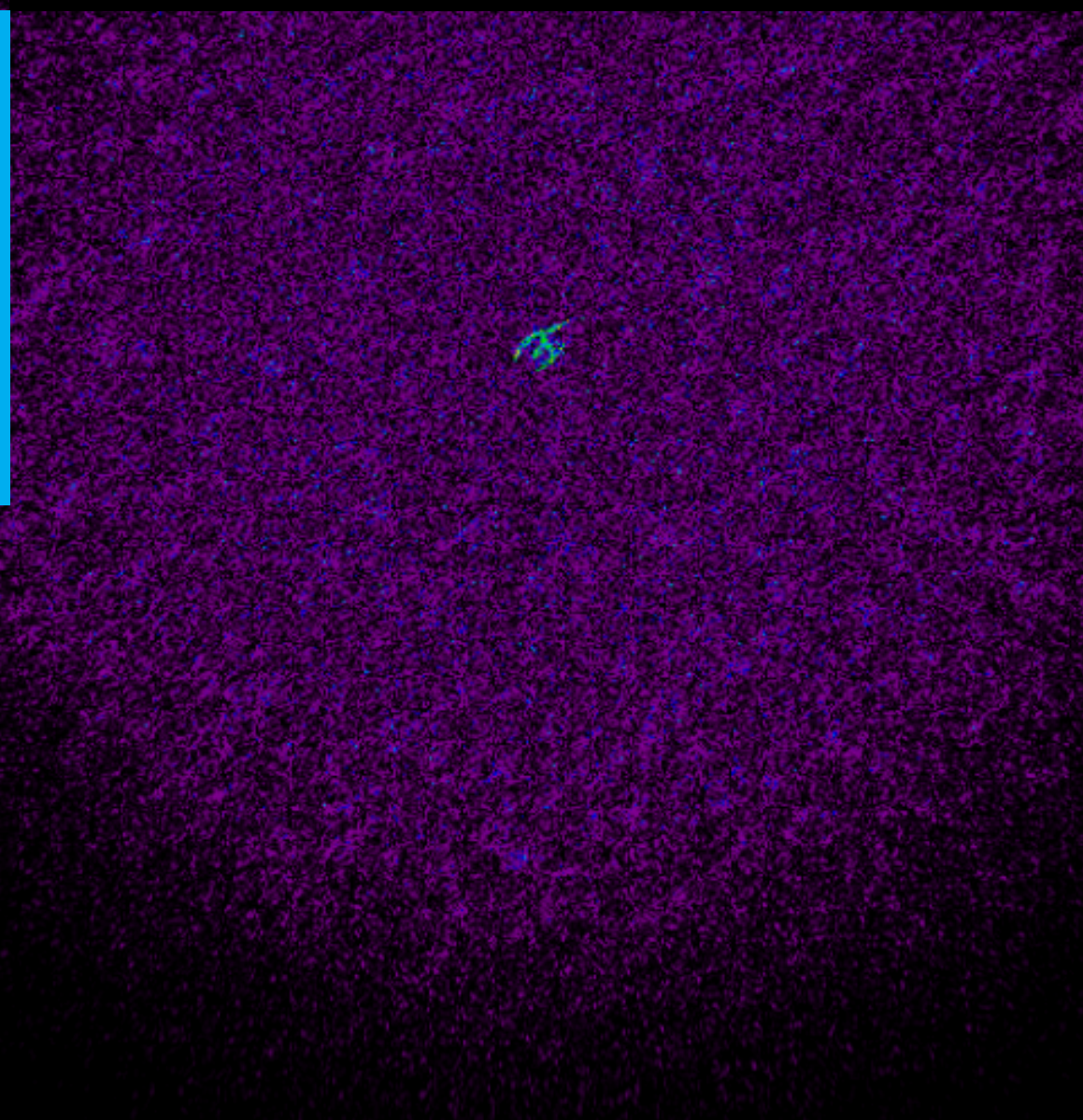


Identification and control of light propagation in optical waveguides

Gijs de Jongh



Identification and control of light propagation in optical waveguides

MASTER OF SCIENCE THESIS

For the degree of Master of Science in Systems and Control at Delft
University of Technology

Gijs de Jongh

October 7, 2016

Faculty of Mechanical, Maritime and Materials Engineering (3mE) · Delft University of
Technology



Copyright © Delft Center for Systems and Control (DCSC)
All rights reserved.



Abstract

Optical fibres are ideal for local light delivery in hard to access places due to their flexible nature and small size. In most applications, such as microscopy, micromanipulation and endoscopy, it is desired to obtain and maintain a specified intensity pattern at the fibre output. Multimode fibres (MMFs) are capable of carrying a large amount information encoded in the complex coefficients of the superimposed propagating transverse modes.

The main obstacle of using MMFs for these purposes is the fact that the small imperfections and impurities in the fibre along with bending causes dispersion and coupling between the modes. As a result the intensity distribution at the fibre output becomes randomised, known as a speckle pattern. The speckle pattern of a stationary fibre is time-invariant and the transmission characteristic of the MMF can be fully described by typically a very large non-sparse complex transmission matrix (TM). However, when the fibre is moved or disturbed the transmission matrix changes making dynamic operation in real time difficult to achieve. A desired output intensity pattern can be obtained by controlling the phase of the light field at the MMF input with a spatial light modulator (SLM). The SLM settings can be computed directly by optimising a specified objective intensity at the MMF output, or by retrieving the TM first and subsequently deduce the associated SLM phases.

In this thesis alternative ways are explored to identify a light transmission model that is able to exploit the high resolution of state of the art spatial light modulators by using intensity measurements only. The proposed methods in this report rely on basis expansions into the fundamental transverse fibre modes, as well as into the Fourier basis, resulting in a significant reduction of the problem's dimensionality. Also an iterative learning control strategy is proposed to compensate for small fibre movements during and after the identification process.

Table of Contents

1	Introduction	1
1-1	Motivation	1
1-2	Wavefront shaping	2
1-2-1	Optimisation based methods	3
1-2-2	Transmission matrix approach	4
1-3	Spatial light modulator	5
1-4	Problem statement	5
1-4-1	The curse of dimensionality	5
1-4-2	Phase ambiguity	6
1-4-3	Contributions	6
2	Transmission Matrix Identification	9
2-1	Introduction	9
2-2	Light propagation in cylindrical waveguides	10
2-2-1	Ray optics	10
2-2-2	Wave optics	11
2-3	Losses and signal distortion	15
2-3-1	Material absorption	15
2-3-2	Scattering	16
2-3-3	Bending	16
2-3-4	Dispersion	16
2-3-5	Birefringence	17
2-4	Modal decomposition	18
2-5	Modal transmission matrix formalism	19
2-6	Phase retrieval	21
2-7	Experiments	25
2-8	Discussion	26

3 Point Spread Function Identification	29
3-1 Model	29
3-2 Relation to Transmission Matrix approach	31
3-3 Alternating projections	32
3-4 Computing the SLM phases	32
3-5 Experiments	34
3-6 Results	35
3-6-1 Demonstration of the principle	36
3-6-2 Test on laboratory setup	38
3-7 Discussion	38
3-7-1 Iterations and image frames	38
3-7-2 Input diversity	39
3-7-3 Effect of sampling	39
3-7-4 Speed of the algorithm	40
4 Control	43
4-1 Rolling window	43
4-2 Iterative Learning Control	44
4-3 Model	44
4-3-1 Discussion	45
5 Conclusions	47
5-1 Main conclusions	47
5-2 Recommendations for future work	48
A Phase Retrieval algorithms	51
B Python Code	57
B-1 Decomposition into transverse modes	57
B-2 Multimode fibre simulation	63
Glossary	71
List of Acronyms	71
List of Symbols	71

List of Figures

1-1	Principle of wavefront shaping [1]	2
1-2	Simulated runs of optimisation policies [2], enhancement as a function of time	3
1-3	Measured runs of optimisation policies [2], enhancement as a function of time	3
1-4	Schematic representation of a multi mode fibre	4
1-5	Schematic representation of experimental setup with reference beam [1]	7
2-1	Propagation of light ray in an optical fibre, [3]	11
2-2	Schematic of low order transverse mode in an optical fibre , [3]	13
2-3	b as a function of V for various LP_{lm} modes, [3]	14
2-4	Transverse intensity pattern of the guided modes of a step index MMF with V-number $V = 8$	15
2-5	Transverse field pattern of the fundamental mode in a curved fibre (macrobend), [3]	16
2-6	Microbends in an optical fibre, [3]	17
2-7	Right side and left side of Eq. (2-27) as a function of b for a fibre with $V = 8$ and $l = 1$. The intersections are numerically computed and the b coordinates are saved.	19
2-8	Modal decomposition of a randomly generated speckle field (left) and reconstruction thereof (right)	20
2-9	Schematic of modal decomposition method. The input field is decomposed into the transverse modes which, by propagation through the fibre, all encounter a mode dependant phase delay. Hence the complex mode coefficients c_1, \dots, c_n of the decomposed input field are multiplied by $\tilde{d}_1, \dots, \tilde{d}_n$ where $ \tilde{d}_1 , \dots, \tilde{d}_n = 1$, and contribute to the output image.	20
2-10	Schematic representation of alternating projection algorithm with compressively stored Γ_n	23
2-11	Running times of phase retrieval algorithms to recover α from $\mathbf{y} = \boldsymbol{\Gamma}\alpha ^2$ as a function of pixel grid size ($M \times M$) for fixed $n_{max} = 18$	26
3-1	Schematic representation of the multiframe alternating projection algorithm for K frames	33

3-2	Experimental setup where the 'SLM plane' is conjugated to the SLM surface and the 'target plane' to the CCD camera. Proper SLM settings would yield constructive interference at the specified location in the target plane	34
3-3	Normalised MSE (left), and running times in seconds (right) of the multiframe deconvolution algorithm for various number of iterations and image frames	35
3-4	Imaging performance, measured as squared euclidean distance between output and target, as a function of input phase standard deviation	36
3-5	Output intensity from the identified PSF (left) and the output intensity from the fibre propagation simulation (middle) after the input phase pattern (right) is given as an input.	36
3-6	Output intensity from the identified PSF (left) and the output intensity from the fibre propagation simulation (middle) after the input phase pattern (right) is given as an input.	37
3-7	Output intensity patterns measured (a): with flat input phase and (b): with optimised phase pattern obtained using the multiframe deconvolution algorithm	38
3-8	Imaging performance, measured as squared euclidean distance between output and target, as a function of input phase standard deviation for three different Spatial Light Modulator (SLM) support lengths	40
3-9	Demonstration of the speed of the multiframe deconvolution algorithm compared to the modal decomposition method of Chapter 2 solved by alternating projections, for different grid sizes.	41
4-1	Block scheme of online identification method with a rolling window	44
4-2	Schematic of the convergence of ILC towards the desired output Y_d by updating the input signal $X(t)$	45

List of Tables

2-1	Gerchberg-Saxton algorithm	22
2-2	Alternating Projections algorithm using the compressed Γ matrix	23
3-1	Multiframe deconvolution by alternating projections	32

Chapter 1

Introduction

The work in this thesis is about the identification of a light propagation model of optical waveguides in general and multi mode optical fibres in particular, and control methodologies that can deal with the changing small changes of transmission characteristics induced by bending. This introductory chapter describes the motivation and background of this research as well as the goals, followed by an outline of the main body of this report.

1-1 Motivation

In recent years there has been a renewed interest in optical fibres for imaging applications due to the technical advances of spatial light modulators, that enables dynamic holographic shaping of the wavefront at video frame rates. Especially for endoscopy it opened up the possibility to decrease the diameter of the endoscope drastically, up to the point where it fits into the cavity of a hollow needle. In endoscopy, microscopy and other imaging applications it is usually desired to generate a specific intensity pattern at the fibre output, typically a focal spot. However, when coherent light is focussed onto the input of a Multi Mode Fibre (MMF) a number of propagation modes are excited and travel to the other end of the fibre where each mode acquires a particular phase delay depending on the fibre length and spatial configuration. The interference of those modes at the fibre output results in a speckle intensity pattern. Also little imperfections in the fibre, e.g. micro bends, impurities etc. causes dispersion and mode coupling resulting in a scrambling of the input wave field. In 2007 Vellekoop et al. [4] demonstrated the possibility to use interference to form a focal spot behind a slab of scattering material by modulation of the incident wavefront with a phase-only Spatial Light Modulator (SLM). This experiment demonstrates that the scattering process is in fact deterministic and time invariant and can be exploited for imaging applications. Optical wave guides can be viewed as scattering media and are, in the same way as the layer of paint, suitable for "wavefront shaping" techniques. However, as opposed to the static layer of scattering material an optical fibre is flexible in nature, and the transmission characteristics greatly depend on its spatial configuration.

1-2 Wavefront shaping

"Wavefront shaping" is a term referring to the active control of the incident wavefront in multiple scattering media. The principle of wavefront shaping is as follows. As depicted in Figure 1-1, light from a coherent source is incident on a scattering sample. While propagating through, the light is subjected to multiple scattering events. The transmitted light interferes at the exit side of the sample and forms a speckle pattern captured by a camera. The incident wavefront can be modulated by a Spatial Light Modulator (SLM) in such a way that, after propagating through the scattering medium, the light constructively interferes at a specified location.

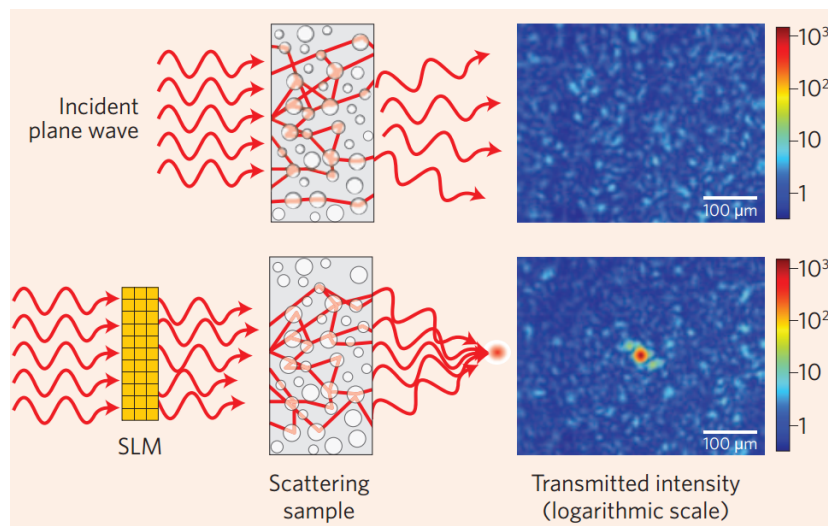


Figure 1-1: Principle of wavefront shaping [1]

Now the question remains: "What should this incident wavefront shape be, that produces the desired output intensity?" There are essentially two approaches to be recognised in literature. The first is by direct optimisation of a certain quality measure, the intensity in a certain region for example, by going through the SLM settings. The pioneering experiment by Vellekoop et al. [4] falls in this category. To make the computations more efficient, the SLM surface could be subdivided into segments where the segment size is changed according to a chosen policy [2] during the optimization. Other research groups soon followed and at first static layers of material were used to form a focus behind [5, 6], but also inside [7, 8] and used to maximise energy transmission through [9, 10] the slab.

The second approach is based on scattering matrix theory [11, 12] which allows for the identification of a mapping between input and output wave fields. This mapping gives a full description of the scattering process and an optimal input field can be deduced from it that produces a given desired output field or intensity. The next sections will treat the optimisation and transmission matrix approach in more detail.

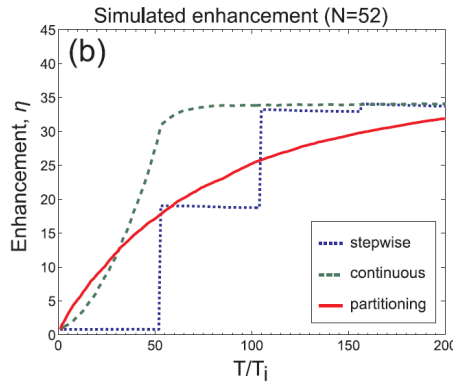


Figure 1-2: Simulated runs of optimisation policies [2], enhancement as a function of time

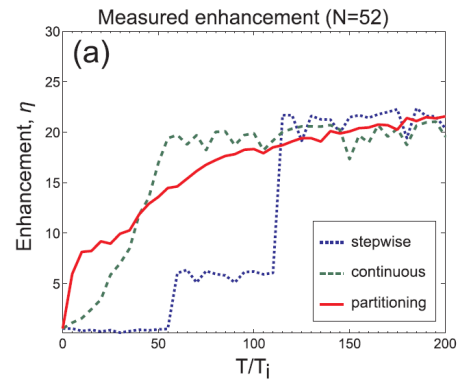


Figure 1-3: Measured runs of optimisation policies [2], enhancement as a function of time

1-2-1 Optimisation based methods

The optimisation algorithms in [2] were applied to a slab of scattering material but can also be applied to a static Multi Mode Fibre (MMF). The paper presents three different optimisation policies: the stepwise sequential, continuous sequential and the partitioning algorithm. In the stepwise sequential algorithm the SLM surface is subdivided into N segments. Then the computer cycles the phase of every segment from 0 to 2π . The output intensity is monitored by the camera and the phase associated with the highest intensity in the target area is stored. After all iterations are performed the optimal phase is set to all segments at once.

The continuous sequential algorithm is very similar to the stepwise sequential algorithm except that the optimal phase for each segment is applied directly after each measurement. Therefore the signal to noise ratio is increased quickly with respect to the stepwise algorithm and it also follows small changes in the medium better.

The partitioning algorithm randomly subdivides the SLM pixels into two subsets. So each subset contains half of the SLM's pixels. Then the target intensity is maximised by changing the phase of one subset with respect to the other. The next iteration a different partitioning is made and the procedure starts again. A fast initial increase of enhancement is obtained by this algorithm which also quickly increases the signal to noise ratio.

A comparison of the three algorithms can be seen in Figure 1-2 and Figure 1-3 for $N = 52$ SLM segments where the enhancement is defined as $\eta = \frac{I_N}{\langle I_0 \rangle}$ with $\langle I_0 \rangle$ the ensemble averaged intensity before optimisation.

It is seen in Figure 1-2 and Figure 1-3 that the continuous sequential and partitioning algorithms show a quick initial gain as expected and that the continuous sequential policy seems to be the fastest.

Also other quality metrics have been proposed as objective functions for random optimisation, see [13] for example. Direct optimisation methods are relatively straight forward and require only an SLM and a camera. The dimensionality of the optimisation problem grows with the number of SLM segments, and becomes very time consuming when the full resolution of state-of-the-art SLMs are used.

1-2-2 Transmission matrix approach

A model-based approach uses the linearity of the scattering process and is denoted as the transmission matrix approach. The scattering occurring in complex media and optical waveguides is a deterministic process that can be modelled using scattering matrix theory [11], [12]. The derivation in this section focusses on an optical fibre but can be extended to any scattering medium [14]. A schematic representation of a MMF is given in Figure 1-4. The incoming and outgoing monochromatic wave fields are denoted by \mathbf{a}_i and \mathbf{b}_i respectively, where $i = 1, 2$ corresponds to the left and right side of the fibre.

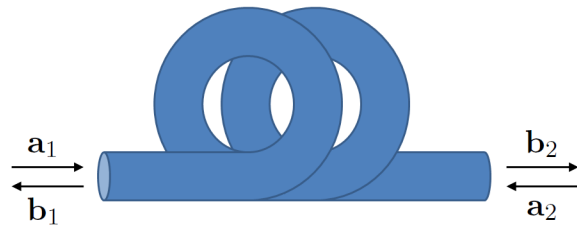


Figure 1-4: Schematic representation of a multi mode fibre

The scattering matrix \mathbf{S} is the linear mapping between incoming and outgoing fields, given as follows.

$$\begin{bmatrix} \mathbf{b}_1 \\ \mathbf{b}_2 \end{bmatrix} = \begin{bmatrix} \mathbf{S}_{11} & \mathbf{S}_{12} \\ \mathbf{S}_{21} & \mathbf{S}_{22} \end{bmatrix} \begin{bmatrix} \mathbf{a}_1 \\ \mathbf{a}_2 \end{bmatrix} \quad (1-1)$$

Since the optical fibre used for most imaging applications are of limited length, losses can be neglected such that optical power is preserved and hence \mathbf{S} is unitary:

$$\mathbf{S}^{-1} = \mathbf{S}^H \quad (1-2)$$

where the superscript H stands for (conjugate transpose). If it is also assumed that the optical fibre is reciprocal then

$$\mathbf{S}^T = \mathbf{S} \quad (1-3)$$

and particularly

$$\mathbf{S}_{21}^T = \mathbf{S}_{12} \quad (1-4)$$

Assuming no interaction between forward and backward propagating fields and vice versa gives:

$$\mathbf{S}_{11} = \mathbf{S}_{22} = \mathbf{0} \quad (1-5)$$

This allows Eq. (1-1) to be decoupled into two equations. Considering only forward propagation, i.e. from side 1 towards 2, the following equation is obtained.

$$\mathbf{b}_2 = \mathbf{S}_{21}\mathbf{a}_1 \quad (1-6)$$

$$\doteq \mathbf{D}\mathbf{a}_1 \quad (1-7)$$

where \mathbf{D} is used to simplify notation and is known as the Transmission Matrix (TM). If the TM can be obtained then, given a desired output field, the corresponding input field can be calculated. The TM is a very large non-sparse complex matrix that fully describes the light transmission inside the fibre. The first measurement of a 256×256 TM of a layer of paint (ZnO) was reported in [15]. Being able to obtain the TM of a MMF enables more freedom in choosing and switching between desired output intensity patterns without the need for extra optimisation. Knowledge of the TM also allows for the use of an optical fibre, or any scattering material for that matter, to be used as a high quality optical element, such as a lens [16], a microscope [17, 18, 19], optical manipulators [20], or in compressive sensing applications [21] for example.

1-3 Spatial light modulator

The Spatial Light Modulator (SLM) is a critical piece of equipment for wavefront shaping techniques. SLMs are diffractive optical elements that modulate a beam of light spatially. It is in essence a dynamic computer controlled transparency. There are various types of light modulators available. They can be divided according to which aspect of the light it modulates, the mechanism it uses to do this, and whether they work transmissive or reflective. The most commonly used type are liquid crystal phase-only reflective SLMs. Liquid crystals are cheap and readily available, and reflective mode is preferred because, compared to transmissive devices, only half of the thickness is needed which therefore halves the switching times. The pixelated surface of the SLM consists of liquid crystals that realign themselves in response to an applied voltage, thereby changing their optical properties. In this way the SLM controls the optical path length of every pixel and induces a specific phase delay at that pixel position. The maximum phase delay an SLM can produce depends on the thickness of the liquid crystal and the wavelength of the light. SLMs working in reflective mode obviously need half the thickness of a transmissive device. Phase-and-amplitude modulators are much more expensive than phase-only devices and are usually not preferred because amplitude modulation removes energy from the beam. However, by constraining the modulation to be phase-only there is often no analytic solution that will yield the desired output pattern. A way to circumvent this is by shaping the amplitude and phase in the Fourier plane of the phase-only hologram. This can for example be done with the Gerchberg-Saxton algorithm [22].

Another type of frequently used light modulator, worth noting, is a so called Digital Micromirror Device (DMD). Every pixel of the DMD is a micro mirror that can be toggled on or off, such that only the field amplitude is modulated in binary way. The switching of the mirror states is quick and operates at speeds > 20 kHz with high pixel counts and increases the speed significantly with respect to an SLM, which operates at roughly 100 Hz.

1-4 Problem statement

1-4-1 The curse of dimensionality

The large number of pixels the SLM together with the high resolution of the camera, gives rise to computational issues. As an example, consider an SLM with $N \times N$ pixels, where

every pixel can take L phase levels between 0 and 2π . Then the number of possible SLM settings P can be calculated as $P = L^{N \times N}$, which very quickly blows up for increasing N . For a typical SLM $N = 512$ and $L = 256$. That means that if the SLM phases is to be optimised with regard to some quality measure of the output intensity, the search space is enormous.

This also has a consequence for the size of the Transmission Matrix (TM). In the TM formulation the input field is mapped by the TM to the output field. In practise this implies a discretisation of the fields. The input field is generated by the SLM and consists of $N \times N$ pixels which are vectorised, yielding a vector $\mathbf{x} \in \mathbb{C}^{N^2 \times 1}$. At the output side a camera detects the intensity with $M \times M$ pixels, which gives a vector $\mathbf{y} \in \mathbb{R}^{M^2 \times 1}$. This subsequently determines the TM dimensions to be $\mathbf{D} \in \mathbb{C}^{M^2 \times N^2}$ which becomes problematic to store in memory of an ordinary consumer computer. Additionally, estimating the TM requires at least N^2 measurements to obtain an overdetermined system of equations. Knowledge about sparsity constraints can lower this number [23, 24, 25] are generally not applicable. Consequently a clear trade-off appears between computational complexity and resolution. Therefore, in most cases found in literature, optimisations [4, 5, 6, 26] and Transmission Matrices calculations [27, 15, 28, 29, 30, 31] are kept tractable by lowering the resolution settings on camera and SLM, at the expense of the desired output intensity pattern quality.

1-4-2 Phase ambiguity

A second difficulty, appearing in the TM approach, is the fact that a CCD camera can only capture intensity images, whereas the complex amplitude is required. The intensity measurement simply loses the important phase information of the complex output field. This turns the linear relation between incoming and outgoing complex valued light fields into a nonlinear one:

$$\mathbf{y} = |\mathbf{D}\mathbf{x}|^2 \quad (1-8)$$

where the squared magnitude is taken element wise, i.e. $y_i = |\mathbf{d}_i \mathbf{x}|^2 = \mathbf{d}_i \mathbf{x} \mathbf{x}^H \mathbf{d}_i^H$, $1 \leq i \leq N$, where y_i and \mathbf{d}_i are respectively the i^{th} element and row of \mathbf{y} and \mathbf{D} . Additionally, when the TM would be known *a priori*, and a specific output *intensity* $\mathbf{y} = \mathbf{y}^*$ is required, the optimal input requires solving the dual problem (Eq. (1-8)), which is known as the phase retrieval problem. Access to the complex amplitude of the output requires holographic measurements [15, 32], i.e. interference with a reference beam as shown in Figure 1-5 . This however demands interferometric stability and increases the complexity of the optical setup significantly.

1-4-3 Contributions

In this thesis work the goal is to find a computational and memory efficient method to estimate the Transmission Matrix of a multi mode optical fibre using high resolution intensity images and phase-only spatial light modulation. In Chapter 2 a decomposition of the complex fields into the transverse fibre modes is proposed to obtain a reduced dimensional problem.

In Chapter 3 a method of modelling the multi mode optical fibre by its Point Spread Function (PSF) is proposed which is identified with a multiframe deconvolution algorithm. Finally

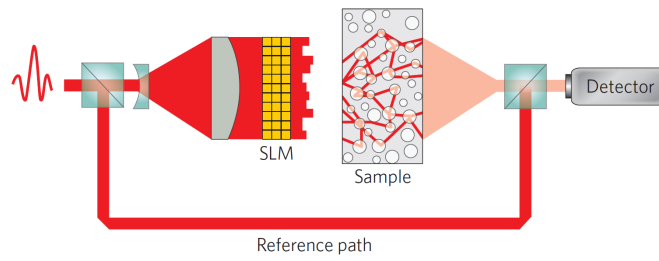


Figure 1-5: Schematic representation of experimental setup with reference beam [1]

the use an Iterative Learning Control (ILC) methodology is investigated to reject small perturbations on the transmission characteristics of the MMF as a result of bending in Chapter 4.

Chapter 2

Transmission Matrix Identification

As discussed in Chapter 1, the large dimensions of the Transmission Matrix (TM) gives rise to a trade off between high resolution and computational complexity, limiting the potentiality of this approach for imaging applications. In this chapter the search for a memory efficient and computational tractable method to compute and store the TM is discussed. The proposed method is based on a orthonormal basis expansion of the complex input and output fields where the basis set consists of fundamental guided transverse modes arising from the model of light propagation in cylindrical waveguides.

2-1 Introduction

The potential of the TM approach is greatly limited by the size of the TM since it forms a nonlinear mapping between Spatial Light Modulator (SLM) and camera pixels, where the nonlinearity stems from the intensity measurement. For clarity this relation is repeated below from Eq. (1-8)

$$\mathbf{y} = |\mathbf{D}\mathbf{x}|^2 \quad (2-1)$$

where again $\mathbf{D} \in \mathbb{C}^{M \times N}$ is the Transmission Matrix, $\mathbf{x} \in \mathbb{C}^N$ is the ingoing complex field and $\mathbf{y} \in \mathbb{R}^M$ is the measured output intensity. Note that the magnitude is taken element wise. In this chapter a method is proposed to shrink the size and density of the TM to allow for high resolution camera and SLM application. The proposed method exploits the theoretical derived transverse mode fields appearing in cylindrical symmetric waveguides, such as optical fibres. As will be derived in the following sections, coherent light incident on a Multi Mode Fibre (MMF) tip will excite a number of propagation invariant modes, specific to the fibre parameters, that will form an interference pattern at the fibre output. Any resulting complex output field $\psi(r, \phi)$ can therefore be decomposed into this complete and finite basis set of transverse modes as follows

$$\psi(r, \phi) = \sum_{n=1}^{n_{max}} c_n \Gamma_n(r, \phi) \quad (2-2)$$

where $\Gamma_n(r, \phi)$ for $n = 1, \dots, n_{max}$ are the transverse modes, weighted by c_n . Then instead of relating discretised input to output fields, which result in a huge non-sparse complex TM, it might be computationally advantageous to relate mode coefficients. This will in the first place shrink the TM dramatically, and secondly, encouraged by work of Bruning et al. [28], it is anticipated that in this formalism the TM will only contain diagonal entries with unit magnitude, giving

$$\mathbf{c}_y = \tilde{\mathbf{D}} \mathbf{c}_x \quad \text{with} \quad \tilde{\mathbf{D}} = \text{diag}(e^{j\tilde{d}_1}, e^{j\tilde{d}_2}, \dots, e^{j\tilde{d}_{n_{max}}}) \quad (2-3)$$

where \mathbf{c}_x and \mathbf{c}_y are input and output mode coefficient vectors, and $\tilde{\mathbf{D}}$ is the diagonal TM. The underlying idea is that every guided mode has a specific propagation velocity, such that the output field is equal to a superposition of the phase-delayed input modes. In non-ideal fibres some inter-modal dispersion effects might occur, energy from one mode might leak into another, resulting in the TM having some off-diagonal entries. However the number of guided modes used in [28] is limited to 10, which is not a realistic scenario for imaging applications, and the proposed method does not seem well suited to scale up to handle large number of modes. Therefore in this chapter an alternative method is sought that can handle realistic numbers of guided modes, ideally without the need for interferometry. First a thorough derivation of light propagation in a step index multimode fibre will be given leading to the definition of the basis $\Gamma_n(r, \phi)$, followed by ways to decompose a given wavefield into its basis modes and finally the calculation of the TM is discussed.

2-2 Light propagation in cylindrical waveguides

2-2-1 Ray optics

An optical fibre typically consists of a core surrounded by a cladding layer of a lower refractive index, both made of dielectric materials. Light is transmitted between the two ends of the fibre by the principle of total internal reflection which makes the fibre act as an optical waveguide. The core refractive index must be higher than the cladding's and the transition can either be abrupt, in step-index fibres, or gradually, typically parabolic in graded-index fibres. The workings of an optical fibre can be intuitively understood by geometrical optics. Light travelling in the optically dense core is totally reflected at the boundary with the cladding if the angle of incidence is greater than the critical angle. In a graded-index optical fibre the light refocused continually resulting in a sinusoidal trajectory of rays. The critical angle is a function of the core and cladding's refractive indices and determines the acceptance angle of the fibre, the Numerical Aperture (NA), as follows.

$$\text{NA} = n_0 \sin(\theta_A) = \sqrt{n_1^2 - n_2^2} \quad (2-4)$$

Usually the light enters the core of the fibre from air such that $n_0 = 1$. The concept of modes propagation in optical waveguides can be intuitively understood as the different zigzagging

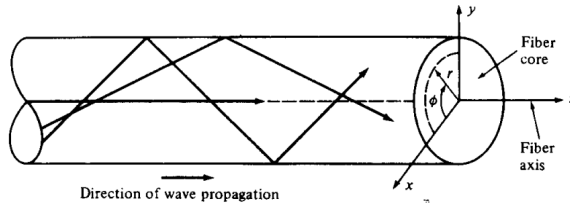


Figure 2-1: Propagation of light ray in an optical fibre, [3]

trajectories a ray can travel through the other end of the fibre, as can be seen in Figure 2-1. For more understanding of light propagation in optical waveguides it is necessary to consider the wave nature of light.

2-2-2 Wave optics

For a wave optic representation of light propagation in optical fibres it is necessary to solve Maxwell's equations subject to cylindrical boundary conditions. An electromagnetic wave propagating in an optical fibre is described in a cylindrical coordinate system as defined in Figure 2-1, where r is the radial coordinate and ϕ the azimuthal angle.

From Maxwell's equations the wave equation in cylindrical coordinates can be derived and is given as:

$$\frac{\partial^2 \Psi}{\partial r^2} + \frac{1}{r} \frac{\partial \Psi}{\partial r} + \frac{1}{r^2} \frac{\partial^2 \Psi}{\partial \phi^2} + \frac{\partial^2 \Psi}{\partial z^2} = \frac{n^2(r)}{c^2} \frac{\partial^2 \Psi}{\partial t^2} \quad (2-5)$$

where $n(r)$ is the radial dependant refractive index of the guiding medium. The following derivation is restricted to a step index fibre, such that $n(r)$ becomes:

$$n(r) = \begin{cases} n_1, & \text{for } 0 < r \leq a \\ n_2, & \text{for } r > a \end{cases} \quad (2-6)$$

The goal is to find the solutions of Eq. (2-5) subject to the boundary conditions opposed by the optical fibre geometry. The solution can be written in the following form.

$$\Psi(r, \phi, z, t) = \psi(r, \phi) e^{j(\omega t - \beta z)} \quad (2-7)$$

Eq. (2-7) describes the wave field as a propagation invariant transverse field pattern $\psi(r, \phi)$ propagating in the z direction with a change in phase with phase velocity $v_p = \omega/\beta$. β is the z component of the propagation vector and will be determined by the boundary conditions later on.

Substituting Eq. (2-7) into Eq. (2-5) gives

$$\frac{\partial^2 \psi}{\partial r^2} + \frac{1}{r} \frac{\partial \psi}{\partial r} + \frac{1}{r^2} \frac{\partial^2 \psi}{\partial \phi^2} + [k_0^2 n^2(r) - \beta^2] \psi = 0 \quad (2-8)$$

where $k_0 = \frac{\omega}{c} = \frac{2\pi}{\lambda_0}$ is the free space wave number. Eq. (2-8) can be solved by the method of separation of variables such that

$$\psi(r, \phi) = R(r)\Phi(\phi) \quad (2-9)$$

Substituting Eq. (2-9) into Eq. (2-7) and multiplying by $\frac{r^2}{R(r)\Phi(\phi)}$ yields

$$\frac{r^2}{R(r)} \frac{d^2R(r)}{dr^2} + \frac{r}{R(r)} \frac{dR(r)}{dr} + r^2[k_0^2 n^2(r) - \beta^2] = -\frac{1}{\Phi(\phi)} \frac{d\Phi^2(\phi)}{d\phi^2} \quad (2-10)$$

Now the left hand side of Eq. (2-10) only depends on the radius r and the right hand side only on the angle ϕ , and are equal to a constant, say l^2 .

Solving the angular part

First the right hand side of Eq. (2-10) is solved as follows

$$\Phi(\phi) = \begin{cases} \cos(l\phi) \\ \sin(l\phi) \end{cases} \quad (2-11)$$

where l must be an integer, $l = 0, 1, 2, \dots$, to ensure that $\Phi(\phi + 2\pi) = \Phi(\phi)$.

Solving the radial part

To solve the radial part, the left hand side of Eq. (2-10) can be written as:

$$r^2 \frac{d^2R(r)}{dr^2} + r \frac{dR(r)}{dr} + \left[\frac{r^2}{a^2} [k_0^2 n^2(r) - \beta^2] a^2 - l^2 \right] R(r) = 0 \quad (2-12)$$

This equation contains the radial dependant refractive index. For step index fibre the core and cladding have refractive indices n_1 and n_2 respectively such that two parameters are defined as follows:

$$[k_0^2 n^2(r) - \beta^2] a^2 = \begin{cases} [k_0^2 n_1^2 - \beta^2] a^2 \doteq U^2, & 0 < r \leq a \text{ (core)} \\ -[\beta^2 - k_0^2 n_2^2] a^2 \doteq -W^2, & r > a \text{ (cladding)} \end{cases} \quad (2-13)$$

Now Eq. (2-12) can be written as

$$r^2 \frac{d^2R(r)}{dr^2} + r \frac{dR(r)}{dr} + \left[\left(\frac{r}{a} U \right)^2 - l^2 \right] R(r) = 0, \quad 0 < r \leq a \text{ (core)} \quad (2-14)$$

$$r^2 \frac{d^2R(r)}{dr^2} + r \frac{dR(r)}{dr} - \left[\left(\frac{r}{a} W \right)^2 + l^2 \right] R(r) = 0, \quad r > a \text{ (cladding)} \quad (2-15)$$

Eq. (2-14) and Eq. (2-15) can be recognised as Bessel's differential equations, which both have two independent solutions. However, only the bounded solution is relevant in this case. So the solutions of Eq. (2-14) and Eq. (2-15) become:

$$R(r) = C_1 J_l \left(\frac{r}{a} U \right) \quad 0 < r \leq a \text{ (core)} \quad (2-16)$$

$$R(r) = C_2 K_l \left(\frac{r}{a} W \right) \quad r > a \text{ (cladding)} \quad (2-17)$$

where C_1 and C_2 are constants that are determined later on and $J_l(\cdot)$ and $K_l(\cdot)$ are l^{th} order Bessel functions of the first and second kind respectively. From this result can be seen that there is an oscillatory field propagating in the core and an exponentially decaying field in the cladding. This is schematically shown in 2-2.

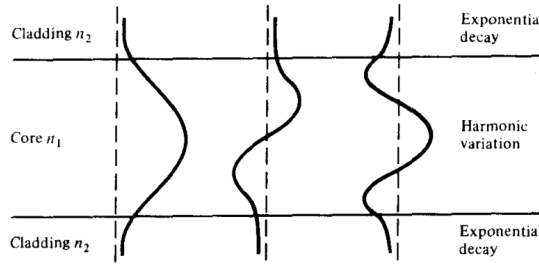


Figure 2-2: Schematic of low order transverse mode in an optical fibre , [3]

Combine results

After combining the intermediate results, (Eq. (2-11) with Eq. (2-16) and Eq. (2-17)) the solution of the wave equation Eq. (2-5) can be written as:

$$\Psi(r, \phi, z, t) = \begin{cases} \frac{C_1}{J_l(U)} J_l \left(\frac{r}{a} U \right) \Phi(\phi) e^{\omega t - \beta z}, & 0 < r \leq a \quad (\text{core}) \\ \frac{C_2}{K_l(W)} K_l \left(\frac{r}{a} W \right) \Phi(\phi) e^{\omega t - \beta z}, & r > a \quad (\text{cladding}) \end{cases} \quad (2-18)$$

The factors C_1 and C_2 are determined from the continuity constraint of wave field, i.e. at $r = a$ the wave equation for the core must equal the cladding's.

The only unknown in Eq. (2-18) is β which can be obtained by the continuity constraint of the wave function's derivative, given as:

$$\frac{U J_{l+1}(U)}{J_l(U)} = \frac{W K_{l+1}(W)}{K_l(W)} \quad (2-19)$$

There are at this point two important dimensionless parameters that need to be defined. First is the normalised frequency V , also called 'V-number', and the second is the normalised propagation constant b .

$$V \doteq k_0 a \sqrt{n_1^2 + n_2^2} \quad (2-20)$$

$$b \doteq \frac{\beta^2 / k_0^2 + n_2^2}{n_1^2 + n_2^2} \quad (2-21)$$

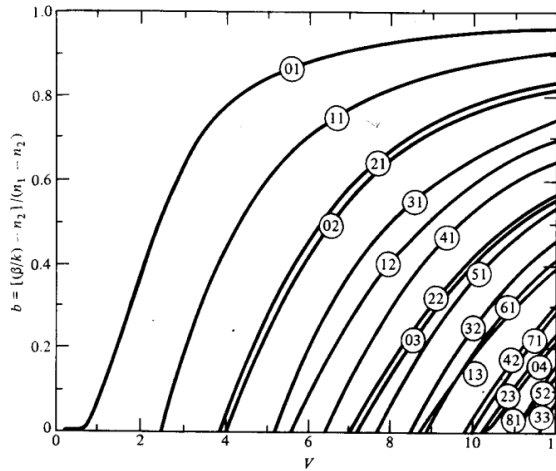
With Eq. (2-20) and Eq. (2-21) U and W can be rewritten in terms of V and b as:

$$U = V\sqrt{1-b} \quad (2-22)$$

$$W = V\sqrt{b} \quad (2-23)$$

So for a given fibre the V-number is known, and b can be calculated from Eq. (2-19), Eq. (2-22) and Eq. (2-23). This has m solutions for every $l = 0, 1, 2, \dots$ which are denoted as LP_{lm} (Linear Polarised) modes. As an example, consider a fibre with $V = 3$. Then for $l = 0$, Eq. (2-19) has only one solution $m = 1$ denoted by LP_{01} . Next, for $l = 1$ Eq. (2-19) also has only one solution: LP_{11} . This means that this particular optical fibre supports the propagation of two modes, namely LP_{01} and LP_{11} .

A plot of the propagation constant b as a function of V is shown in Figure 2-3 where the numbers on the curves in Figure 2-3 represent the LP_{lm} modes. It can be seen that for values of $V < 2.4$ only one solution can be found which means only one mode is supported by the fibre (LP_{01}). Optical fibres in this domain are called single mode fibres. As V increases, by increasing the core radius for example, more modes are supported which is the domain of multi mode fibres. The V-number at which a certain mode is no longer supported, is called the cutoff condition. In terms of ray optics this can be understood as the angle of incidence at which there is no total internal reflection and the ray escapes into the cladding. Note that every linear polarised mode consists of two possible polarisation directions. In the case of a perfectly homogeneous and cylindrical symmetric fibre the propagation constants are the same.



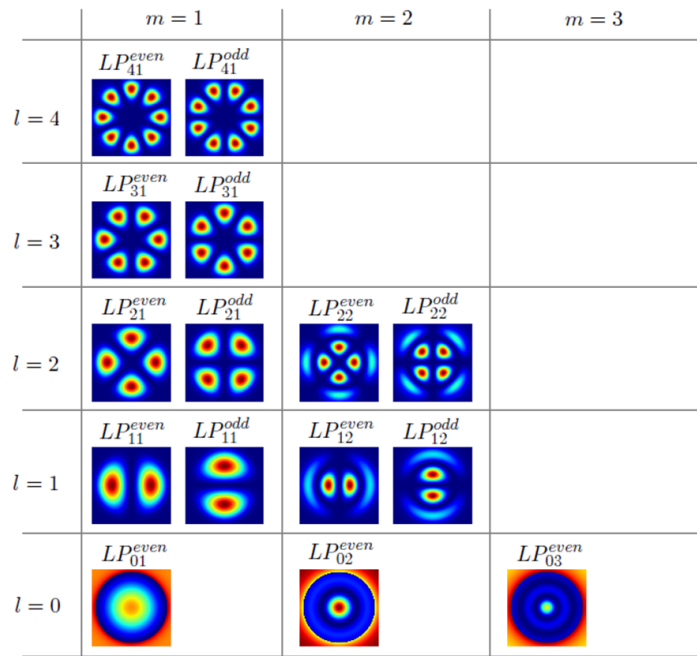


Figure 2-4: Transverse intensity pattern of the guided modes of a step index MMF with V-number $V = 8$

2-3 Losses and signal distortion

In the previous section light transmission in an optical fibre was considered for an ideal, perfectly straight fibre. In reality however, material impurities, micro bends, geometrical imperfections, etc, result in various kinds of losses and distortions of the propagating light. The following types of loss mechanisms are described.

- material absorption
- scattering
- bending
- dispersion

2-3-1 Material absorption

Material absorption is a loss mechanism related to the material composition the fibre and can be subdivided into intrinsic and extrinsic absorption. Intrinsic absorption occurs due to electronic absorption bands within the glass material in the ultraviolet region and also molecular vibration in the infrared region. Extrinsic absorption losses are caused by impurities injected during the fabrication process. Most undesired impurities are metal ions and OH^- ions. The metal ion concentration is very critical and must be kept below one part per billion (ppb).

2-3-2 Scattering

Another phenomenon deteriorating the fibre's transmission is scattering which arises from microscopic variations in density with associated refractive index. Rayleigh scattering is caused when the fibre material anomaly is small compared to the wavelength and a small part of the optical ray can escape into the cladding.

2-3-3 Bending

Radiative loss also occurs when the fibre is bend. A fibre can undergo two types of bends. The first type is when the radius of curvature is large compared to the fibre diameter, denoted as macrobends. This is, for example, when the fibre turns a corner. The curvature loss effects can be examined qualitatively from the modal distribution, see Figure 2-5. As explained previously, the transverse mode tail extends in the cladding. As the fibre is bend the tail on the outside must propagate faster to keep up with the field in the core. At a certain critical distance, x_c in Figure 2-5, the light would have to travel faster than the speed of light, which is not possible. The amount of radiation losses caused by bending depends thus on the field strength at x_c and the radius of curvature R . Microbends result in radiation losses because of mode coupling. Energy of one mode is coupled to guided higher order modes or non-guided leaky modes. The total number of modes that can be supported by a curved fibre is therefore less than a in a straight fibre. A more detailed analysis on radiation losses in curved optical fibres can be found in [33] and the references therein.

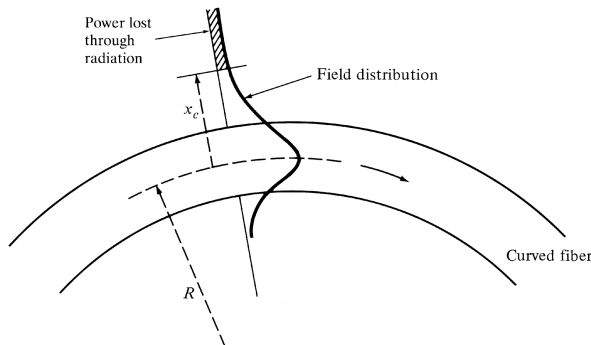


Figure 2-5: Transverse field pattern of the fundamental mode in a curved fibre (macrobend), [3]

A second type of bending is caused by random microbends. Microbends are small random fluctuations in the radius of curvature of the fibre as shown in Figure 2-6. They are induced into the fibre during the fabrication process, mainly caused by temperature variations.

2-3-4 Dispersion

The signal also gets distorted while it propagates. This is caused by intramodal and intermodal dispersion effects. Intramodal dispersion is the pulse spreading that occurs within a single mode and is caused by material dispersion and waveguide dispersion. Material dispersion is caused by variations in refractive index in the core material and is also known as chromatic dispersion. A light source rarely emits light of exactly one wavelength which

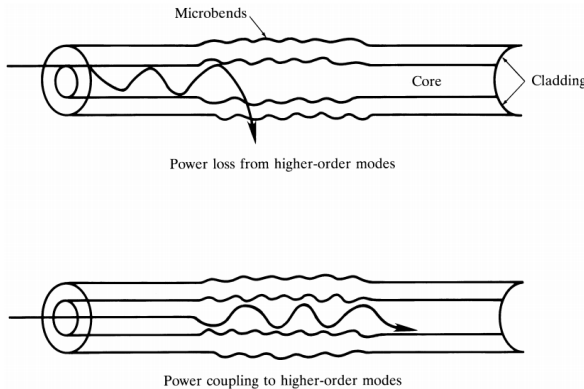


Figure 2-6: Microbends in an optical fibre, [3]

causes a wavelength dependence of the group velocity of a particular mode. So intramodal dispersion also occurs when different wavelengths follow the same path. The second source of intramodal dispersion, waveguide dispersion, is due to the fact that the light in fibre cladding travels faster than in the core. And since part of the modal energy travels in the cladding the mode is dispersed. In multi mode fibres intermodal dispersion is a result each mode having a different group velocity. This a major reason why single mode fibres are predominantly used for communication applications.

2-3-5 Birefringence

Another source of dispersion is caused by random polarization properties of the fibre. The fibre can thus act as birefringent medium, such that a certain polarisation direction travels faster through the fibre. Polarization modal dispersion is orders of magnitude less than chromatic dispersion but can be the limiting factor when fibres with dispersion compensators are used. Optical fibres with cylindrical cores favours one polarisation state and can be useful if a certain polarization is to be maintained.

2-4 Modal decomposition

Starting again from Eq. (2-7), repeated in Eq. (2-24) below for clarity, the propagating field $\psi(r, \phi)$ can be regarded as a superposition of a set of orthogonal LP_{lm} modes (Eq. (2-25)), denoted by $\Gamma_n(r, \phi)$. Note that all modes are normalised to have unit power.

$$\Psi(r, \phi, z, t) = \psi(r, \phi)e^{j(\omega t - \beta z)} \quad (2-24)$$

$$\psi(r, \phi) = \sum_{n=1}^{n_{max}} c_n \Gamma_n(r, \phi) \quad (2-25)$$

The number of guided modes of a MMF is dependant on the V-number and is approximated [34] by

$$n_{max} \approx \frac{V^2}{2} \quad (2-26)$$

To achieve high resolution images at the output of the fibre a high NA is desired and therefore, the higher the V-number the better. Also in terms of modes, the higher order modes determine the level of detail that can be achieved in the output image. However, a high V-number comes at the cost of computational time, to do the modal expansion, and memory issues when all modes have to be stored individually. The smallest MMF currently available in the optics lab, for example, has a V-number of $V = 138$ which corresponds to having roughly 9500 guided modes. Having to save all these modes as 512×515 images on a PC requires too much memory. It is therefore chosen to store all transverse modes in a compressed form, by their normalised propagation constant b , and reconstruct the mode fields "on the go". The propagation constants can be calculated *a priori* as follows.

Substituting $U = V\sqrt{1-b}$ (Eq. (2-22)) and $W = V\sqrt{b}$ (Eq. (2-23)) into Eq. (2-19) gives

$$\frac{V\sqrt{1-b}J_{l+1}(V\sqrt{1-b})}{J_l(V\sqrt{1-b})} = \frac{V\sqrt{b}K_{l+1}(V\sqrt{b})}{K_l(V\sqrt{b})} \quad (2-27)$$

where b , the normalised propagation constant, is the only unknown variable. Solving Eq. (2-27) for b , for every l , yields m solutions, corresponding to the LP_{lm} modes. So again, every mode is fully characterised by its corresponding b value, which is calculated numerically from Eq. (2-27).

The left and right sides of Eq. (2-27) are both plotted in Figure 2-7 as a function of b for a MMF with $V = 8$. By definition, recall Eq. (2-21), we have that $0 < b < 1$.

For a given fibre the values of b are calculated *a priori* and requires very little storage capacity. Subsequently a specific transverse mode field $\psi(r, \phi)$ is reconstructed from:

$$\psi(r, \phi) = R(r)\Phi(\phi) \quad (2-28)$$

$$R(r) = \begin{cases} \frac{J_l(\frac{r}{a}U)}{J_l(U)} & 0 < r \leq a \text{ (core)} \\ \frac{K_l(\frac{r}{a}W)}{K_l(W)} & r > a \text{ (cladding)} \end{cases} \quad \text{and} \quad \Phi(\phi) = \begin{cases} \cos(l\phi) \\ \sin(l\phi) \end{cases} \quad (2-29)$$

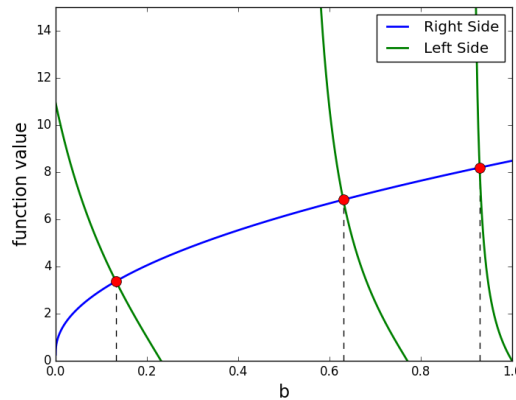


Figure 2-7: Right side and left side of Eq. (2-27) as a function of b for a fibre with $V = 8$ and $l = 1$. The intersections are numerically computed and the b coordinates are saved.

Calculation of the modal coefficients

The modal coefficients defining the contribution of every mode in the total complex field are given by

$$c_n = \rho_n e^{j\theta_n} = \langle \Gamma_n, \psi \rangle = \sum_{i,j} \Gamma_n^*(i,j) \psi(i,j) \quad (2-30)$$

where the sum is taken over all pixels, indexed with i and j . The coefficients c_n fulfil the relation:

$$\sum_{n=1}^{n_{max}} |c_n|^2 = \sum_{n=1}^{n_{max}} \rho_n^2 = 1 \quad (2-31)$$

Given a complex field, the coefficients c_n are calculated with Eq. (2-30) where $\Gamma_n(i,j)$ is computed numerically on the go as explained in previous sections.

As an example a specific complex field is specified, in this case Prometheus' flame of the TU Delft logo as magnitude with a random phase, as shown on the left in Figure 2-8. This field is then decomposed into a set of 4502 basis modes, which corresponds to a fibre with a V-number $V = 138$. The resulting reconstructed amplitude is shown in the right image in Figure 2-8. It can be seen that the number of modes is not sufficient to reproduce the fine details and sharp edges. A bigger diameter fibre, with higher V-number will probably give better results.

2-5 Modal transmission matrix formalism

Coming back to the beginning of this chapter, it was anticipated that, given the decomposed input and output complex fields, the following relation holds.

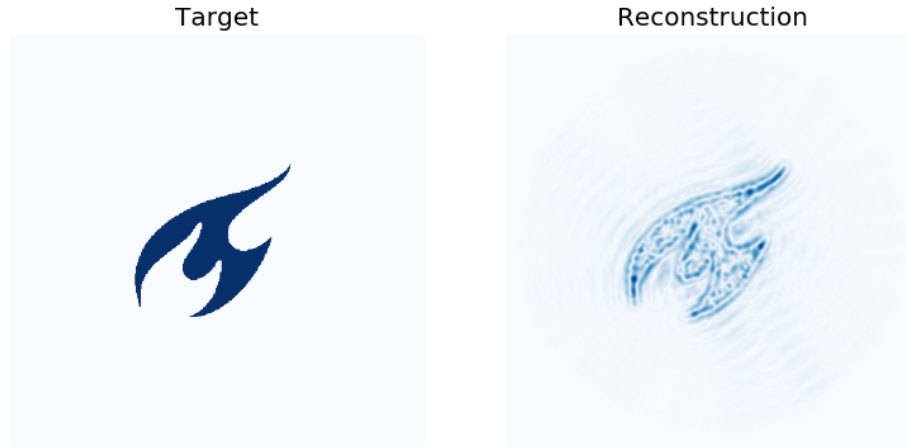


Figure 2-8: Modal decomposition of a randomly generated speckle field (left) and reconstruction thereof (right)

$$\mathbf{c}_y = \tilde{\mathbf{D}}\mathbf{c}_x \quad \text{with} \quad \tilde{\mathbf{D}} = \text{diag}(e^{j\tilde{d}_1}, e^{j\tilde{d}_2}, \dots, e^{j\tilde{d}_{n_{max}}}) \quad (2-32)$$

Hence if, by interferometric methods, the phase and amplitude of the output field could be accessed, and are decomposed into its transverse modes, the relation in Eq. (2-32) can be used straightforwardly to obtain the diagonal TM $\tilde{\mathbf{D}}$. This is schematically shown in Figure 2-9.

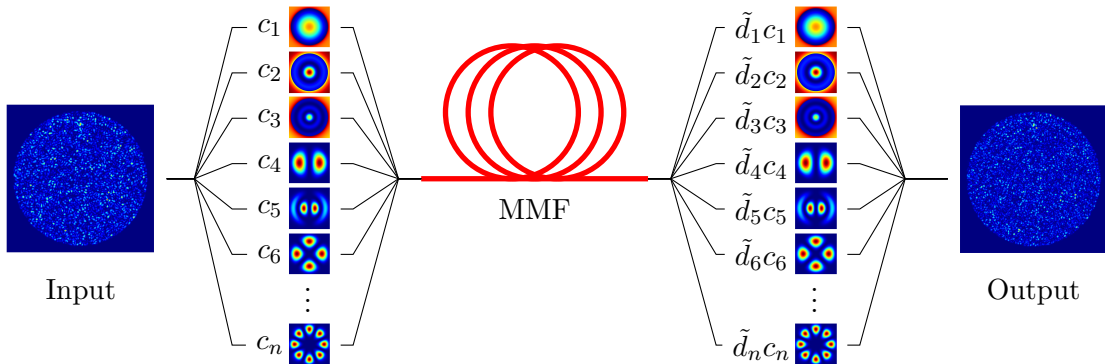


Figure 2-9: Schematic of modal decomposition method. The input field is decomposed into the transverse modes which, by propagation through the fibre, all encounter a mode dependant phase delay. Hence the complex mode coefficients c_1, \dots, c_n of the decomposed input field are multiplied by $\tilde{d}_1, \dots, \tilde{d}_n$ where $|\tilde{d}_1|, \dots, |\tilde{d}_n| = 1$, and contribute to the output image.

However, when only intensity measurements are available, the estimation of $\tilde{\mathbf{D}}$ becomes significantly more involved. Note that due to the coherence of the light source we have that

$$|y(r, \phi)|^2 = \left| \sum_{n=1}^{n_{max}} c_n \Gamma_n(r, \phi) \right|^2 \neq \sum_{n=1}^{n_{max}} |c_n \Gamma_n(r, \phi)|^2 \quad (2-33)$$

thus we can not simply state that $\mathbf{c}_y = |\tilde{\mathbf{D}}\mathbf{c}_x|^2$, where \mathbf{c}_x and \mathbf{c}_y are column vectors containing

the modal coefficients of the input and output fields respectively, and solve this reduces size phase retrieval problem. Instead the following relation holds

$$\mathbf{y} = |\boldsymbol{\Gamma}\tilde{\mathbf{D}}\mathbf{c}_x|^2 \quad (2-34)$$

where $\boldsymbol{\Gamma}$ is the dictionary matrix where its n_{max} columns contain vectorised transverse fibre modes, and the squared magnitude is again element wise.

Eq. (2-34) can be rewritten as

$$\mathbf{y} = |\boldsymbol{\Gamma}\boldsymbol{\alpha}|^2, \quad \text{with } \boldsymbol{\alpha} = \tilde{\mathbf{D}}\mathbf{c}_x \quad (2-35)$$

Calculation of the TM

From Eq. (2-35), $\tilde{\mathbf{D}}$ can be obtained by calculating (the phase of) $\boldsymbol{\alpha}$ first and subtracting the phase of \mathbf{c}_x . Eq. (2-35) very much resembles the conventional TM formalism of Eq. (2-1). The measured intensity \mathbf{y} is equal to the squared modulus of the product of a very large dictionary matrix with a vector. There are, however, some important differences.

The first is that in Eq. (2-35) the dictionary is known *a priori* and can be saved in compressed form. Also the size of the dictionary $\boldsymbol{\Gamma} \in \mathbb{R}^{M^2 \times n_{max}}$ is reduced with respect to $\mathbf{D} \in \mathbb{C}^{M^2 \times N^2}$ in Eq. (2-1), i.e. the number of columns are reduced.

Probably the most important difference is the reduction of the number of unknowns, the elements of $\mathbf{D} \in \mathbb{C}^{M^2 \times N^2}$ versus $\boldsymbol{\alpha} \in \mathbb{C}^{n_{max}}$ since $n_{max} \ll M^2N^2$. It is important to note that to retrieve \mathbf{D} , without further sparsity constraints, at least N^2 measurements are required to obtain an overdetermined system, whereas $\tilde{\mathbf{D}}$ could theoretically be obtained with just a single measurement. More measurements will obviously increase the accuracy. So in the conventional TM formulation this implies that at least N^2 phase retrieval problems have to be solved as opposed to just one in the decomposed system. Even though the compression and decompression of the columns of $\boldsymbol{\Gamma}$ are computational relatively expensive the benefit of the basis expansion approach on the overall TM retrieval remains computationally more efficient for high resolution settings.

2-6 Phase retrieval

The inevitably missing phase information of the complex vector $\boldsymbol{\alpha}$ in Eq. (2-35) (or \mathbf{x} in Eq. (1-8)), due to the camera's intensity measurement, is an often recurring issue in optics. Reconstruction of this complex vector given only measurements of its (linearly transformed) magnitude, such as Eq. (2-35), is a non-convex optimisation problem, notoriously difficult to solve. It is what is known in literature as the "phase recovery" or "phase retrieval" problem. Note that for a given $\boldsymbol{\alpha}$ in Eq. (2-35) the intensity measurement is not unique, since $c\boldsymbol{\alpha}$, with $c \in \mathbb{C}$ and $|c| = 1$, will result in the same intensity pattern. Therefore the signal $\boldsymbol{\alpha}$, or equivalently the phase of \mathbf{y} , can only be recovered up to global phase constant. This will obviously have no consequence since this piston mode is unobservable anyhow.

There are numerous algorithms developed to solve the phase retrieval problem and in the next sections three most prominent approaches found in literature are discussed with application to solving Eq. (2-35), namely the Gerchberg-Saxton algorithm [22], PhaseLift [35, 36] and PhaseCut [37], and prVBEM [38]. A comparison is made between these algorithms in terms of computational time, as this is the main bottleneck in solving Eq. (2-35). In the following sections the different algorithms are simply stated where in Appendix A more elaborate derivations of PhaseLift, PhaseCut and prVBEM are given. This solely serves as background information for comprehension of the algorithms, but for more details it is recommended to consult the corresponding cited literature.

Gerchberg-Saxton Algorithm

The first widely used phase retrieval algorithm was proposed by Gerchberg and Saxton [22], hereinafter referred to as GS algorithm. The algorithm is iterative and based on projections and consists of the steps shown in Table 2-1.

Table 2-1: Gerchberg-Saxton algorithm

Required	$\mathbf{c}_x, \mathbf{y} , i_{max}$	
Initialise	$\hat{\boldsymbol{\alpha}}, i \leftarrow 1$	
repeat		
1.	$\hat{\mathbf{y}} \leftarrow \mathbf{\Gamma} \hat{\boldsymbol{\alpha}}$	Transform the current estimate
2.	$ \hat{\mathbf{y}} \leftarrow \mathbf{y} $	Impose magnitude constraint on $\hat{\mathbf{y}}$
3.	$\hat{\boldsymbol{\alpha}} \leftarrow \mathbf{\Gamma}^\dagger \hat{\mathbf{y}}$	Inverse transform
4.	$ \hat{\boldsymbol{\alpha}} \leftarrow \mathbf{c}_x $	Impose magnitude constraint on $\hat{\boldsymbol{\alpha}}$
5.	$i \leftarrow i + 1$	
until	$i > i_{max}$	

The speed of the algorithm is determined by the two transformation steps every iteration, giving a time complexity scaling as $\mathcal{O}((M^2)^2)$ per iteration, where M^2 is the number of camera pixels. However, the algorithm requires $\mathbf{\Gamma}$ to be stored in computer memory and, in regards to the scale of matrix $\mathbf{\Gamma}$ for realistic CCD pixel counts, is infeasible.

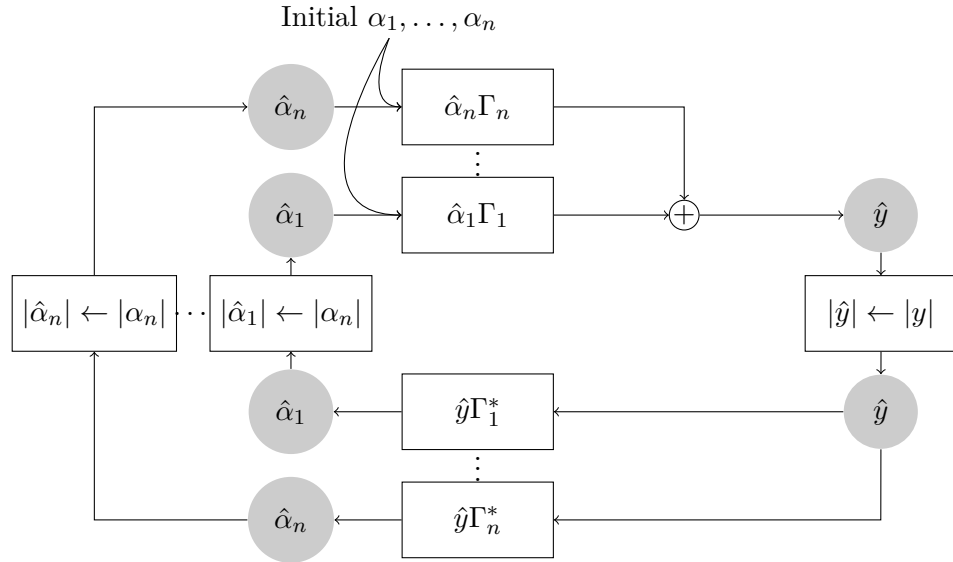
The form of the GS algorithm lends itself well to handle the proposed compressed version of $\mathbf{\Gamma}$ such that memory issues can be resolved. This obviously comes at the cost of extra computations every iteration. The algorithm is summarised in the steps shown in Table 2-2.

The compressed version of GS, differs from the original algorithm only in the way it performs the linear transformations (step 1 and 3). The matrix-vector product is nothing more than a linear combination of the columns of $\mathbf{\Gamma}$ weighted by the elements of $\boldsymbol{\alpha}$. In the compressed GS the columns of $\mathbf{\Gamma}$ are stored compressively, and are evoked on the go. The alternating projections algorithm is shown schematically in Figure 2-10.

Convergence is guaranteed for the GS algorithm [39], however since the constraints are non-convex the algorithm will easily get stuck in local minima. A modified version of the GS algorithm was proposed by Fienup [40] to overcome some of these stagnation problems. However, it is apparent at this point that the biggest disadvantage of the algorithm, with regard to problem at hand, is that each projection step is computationally demanding, due to the size of $\mathbf{\Gamma}$.

Table 2-2: Alternating Projections algorithm using the compressed Γ matrix

Required	$ y(r, \phi) , \mathbf{c}_x, i_{max}$	
Initialise	$\hat{\alpha}_n \quad \forall n = 1, \dots, n_{max}, i \leftarrow 1$	
repeat		
for $n = 1, 2, \dots, n_{max}$		
1.	$\hat{y}(r, \phi) \leftarrow \hat{y}(r, \phi) + \hat{\alpha}_n \Gamma_n(r, \phi)$	Transform the current estimate
2.	$ \hat{y}(r, \phi) \leftarrow y(r, \phi) $	Impose magnitude constraint on $\hat{y}(r, \phi)$
for $n = 1, 2, \dots, n_{max}$		
3.	$\hat{\alpha}_n \leftarrow \langle \Gamma_n(r, \phi), \hat{y}(r, \phi) \rangle$	Inverse transform
4.	$ \hat{\alpha}_n \leftarrow c_{x,n} $	Impose magnitude constraint on $\hat{\alpha}_n$
5.	$i \leftarrow i + 1$	
untill	$i > i_{max}$	

**Figure 2-10:** Schematic representation of alternating projection algorithm with compressively stored Γ_n

Semidefinite programming

An alternative way to solve the phase retrieval problem is based on a convex relaxation. The method starts by observing that Eq. (2-35) describes a set of quadratic relations that can be rewritten as linear equations in a higher dimension, resulting in the following semidefinite programming problem:

$$\begin{aligned} \min \quad & \text{Tr}(\mathbf{A}) \\ \text{s.t.} \quad & y_i = \text{Tr}(\mathbf{Y}_i \mathbf{A}), \quad i = 1, 2, \dots, M^2 \quad (\text{PhaseLift}) \\ & \mathbf{A} \succeq 0. \end{aligned} \quad (2-36)$$

where $\mathbf{A} = \boldsymbol{\alpha} \boldsymbol{\alpha}^H$ and $\mathbf{Y}_i = \boldsymbol{\gamma}_i^H \boldsymbol{\gamma}_i$ with $\boldsymbol{\gamma}_i$ is the i^{th} row of $\mathbf{\Gamma}$. This is a convex problem for which many off-the-shelf numerical solvers exist. Eq. (2-36) is what is known as the "PhaseLift"

algorithm [35, 36].

An alternative approach is taken in [37]. The algorithm proposed, called "PhaseCut", is based on the MaxCut algorithm [41] and separates \mathbf{y} into an amplitude component and a phase component, such that $\boldsymbol{\Gamma}\boldsymbol{\alpha} = \text{diag}(\mathbf{y})\mathbf{u}$, where $\mathbf{u} \in \mathbb{C}^{M^2}$ is a phase vector satisfying $|u_i| = 1$. The PhaseCut algorithm is also formulated as a semidefinite programming problem and becomes:

$$\begin{aligned} \min \quad & \text{Tr}(\mathbf{U}\mathbf{M}) \\ \text{s.t.} \quad & \text{diag}(\mathbf{U}) = 1 \quad (\text{PhaseCut}) \\ & \mathbf{U} \succeq 0 \end{aligned} \quad (2-37)$$

with Where $\mathbf{M} = \text{diag}(\mathbf{y}^T)(\mathbf{I} - \boldsymbol{\Gamma}\boldsymbol{\Gamma}^\dagger)\text{diag}(\mathbf{y})$ and $\mathbf{U} = \mathbf{u}^H\mathbf{u}$.

Both PhaseLift and PhaseCut minimise the trace norm of a large scale complex matrix, $n_{max} \times n_{max}$ for PhaseLift and $N^2 \times N^2$ for PhaseCut. While the PhaseCut problem is larger than PhaseLift, the constraints are singletons which allows for efficient solving. Nonetheless are the matrix dimensions intractable for the given problem and because the algorithms can not be adapted to the proposed compressive framework, they will give rise to memory capacity problems.

Bayesian estimation

The nonlinearity of the modulus can be circumvented by a Bayesian point of view, first proposed in [24]. In this paper the focus is on compressive sensing where the underlying signal, $\boldsymbol{\alpha}$ in this case, is assumed to be sparse. The algorithm is based on 'loopy believe propagation', and in particular the "Generalised Approximate Message Passing" (GAMP) algorithm from [42]. Shortly after, in [38], phase retrieval for a full non-sparse signal was proposed by following a Bayesian variational approach based on a mean field approximation, called phase retrieval Variational Bayesian Expectation Maximisation (prVBEM). In [27] a Transmission Matrix (TM) of size 900 by 40000 was estimated with the this algorithm.

Eq. (2-35) is reinterpreted in the Bayesian approach where the missing phase in the measurement vector is introduces as a new variable. Every absolute valued (pixel) measurement y_μ , $\mu = 1, 2, \dots, M^2$ is thus modelled as

$$y_\mu = e^{j\theta_\mu} \left(\sum_{i=1}^{N^2} \gamma_{\mu,i} \alpha_i + n_\mu \right) \quad (2-38)$$

The missing phase is denoted by $\theta_\mu \in [0, 2\pi)$ and n_μ is a zero-mean circular Gaussian noise with variance σ_n^2 . Note that the subscript μ is used, as opposed to j in previous notation, to distinguish it from the complex $j = \sqrt{-1}$. $\gamma_{\mu,i}$ is the i^{th} element in the μ^{th} row of $\boldsymbol{\Gamma}$ and α_i is the i^{th} element of $\boldsymbol{\alpha}$

In the Bayesian approach the signals are assumed to be realisations of random variables. The probability densities corresponding to the variables are supposed to be

$$p(\boldsymbol{\alpha}) = \prod_{i=1}^{N^2} p(\alpha_i) \quad \text{with} \quad p(\alpha_i) = \mathcal{CN}(0, \sigma_\alpha^2) \quad (2-39)$$

$$p(\boldsymbol{\theta}) = \prod_{\mu=1}^{M^2} p(\theta_\mu) \quad \text{with} \quad p(\theta_\mu) = \frac{1}{2\pi} \quad (2-40)$$

The solution of $\boldsymbol{\alpha}$ is sought via the Maximum A Posteriori (MAP) estimation

$$\hat{\boldsymbol{\alpha}} = \operatorname{argmax}_{\boldsymbol{\alpha}} p(\boldsymbol{\alpha}|\mathbf{y}) \quad (2-41)$$

which is found iteratively using the variational mean-field approximation. This algorithm does not make any hard decisions on values of $\boldsymbol{\alpha}$ at each iteration but computes probabilities. It takes, to some extend, the model uncertainties into account, and refines this model at each iteration before taking a final decision on the values of $\boldsymbol{\alpha}$. The algorithm shares the same time complexity per iteration as the Gerchberg-Saxton algorithm but shows to be more robust to noise [38]. Unfortunately does this algorithm take the full matrix $\boldsymbol{\Gamma}$ as an input does it not adaptable to the proposed compressive framework.

2-7 Experiments

In this section the performance of the phase retrieval algorithms are compared in terms of computational time to solve Eq. (2-35) in computer simulations, namely: prVBEM [38], PhaseCut [37] and Gerchberg-Saxton [22] in both compressed as conventional form. In the experiment a few-mode fibre with V-number $V = 8$ is simulated which has only 18 guided modes ($n_{max} = 18$). For most imaging applications this is not sufficient but it serves well an example where computations remain tractable and allow $\boldsymbol{\Gamma}$ to be stored as a whole as is required for prVBEM and PhaseCut.

The implementations of PhaseCut and prVBEM used in the simulations are proposed by their authors and distributed via their web pages [43, 44]. The algorithms have different complexities. The implementation of PhaseCut relies on a interior point method, derived in [45], where the complexity grows as $\mathcal{O}((M^2)^{3.5}\log(1/\epsilon))$ [37] where ϵ is the target precision. The default stopping criterion is when the ϵ drops below 10^{-2} . The Gerchberg-Saxton algorithm and prVBEM have a similar complexity scaling as $\mathcal{O}((M^2)^2)$ per iteration [38] however the compressive GS algorithm is implemented such that it uses the compressed dictionary matrix $\boldsymbol{\Gamma}$ which obviously requires extra computations. The prVBEM default stopping criterion is when the Kullback-Leibler divergence (see Appendix A) drops below 10^{-8} or after 400 iterations. The GS algorithm stops after 50 iterations as considered a good trade-off between computational time and accuracy.

In the experiment the running times of the four algorithms are measured as a function of the number of camera pixels, i.e. the number of rows of $\boldsymbol{\Gamma}$. The number of columns equals the number of guided modes; in this case 18. The CCD camera is assumed square with pixel grid size ($M \times M$). The running times are measured for $M = 2^p$ for $p = 3, 4, \dots, 9$,

i.e. $M = 8, 16, 32, 64, 128, 256, 512$. The vector $\alpha = \tilde{\mathbf{D}}\mathbf{c}_x$ is generated randomly, and the 'measured' output intensity is computed as $\mathbf{y} = |\boldsymbol{\Gamma}\alpha|^2$. The running times are measured while the algorithms recover α given the intensity \mathbf{y} and $\boldsymbol{\Gamma}$.

It is difficult to have a fair comparison of the running times of algorithms with different stopping criteria. It does however display a general trend how the algorithms perform in high dimensional problems. Figure 2-11 shows the results of the simulations.

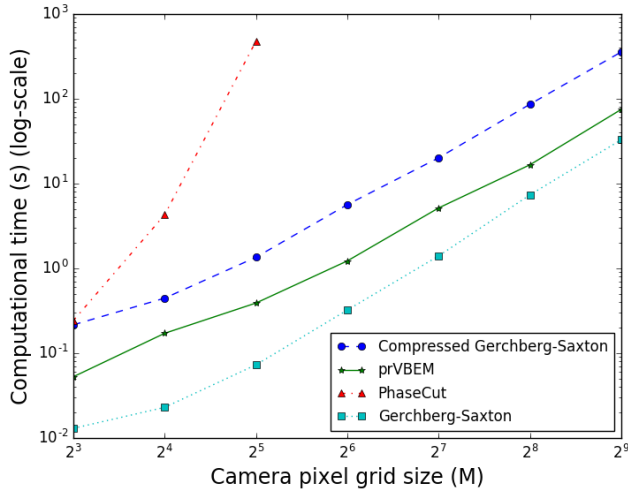


Figure 2-11: Running times of phase retrieval algorithms to recover α from $\mathbf{y} = |\boldsymbol{\Gamma}\alpha|^2$ as a function of pixel grid size ($M \times M$) for fixed $n_{max} = 18$

It can be seen that prVBEM and GS share similar scaling whereas the running time of PhaseCut quickly grows and was able to compute α up to a (32×32) grid after which 'out of memory' errors occur. The compressive Gerchberg-Saxton algorithm shows to be slower with respect to its conventional form, as expected, but outperforms PhaseCut even for very small grid sizes. Arguably, by changing the stopping criteria the crossover point can be shifted somewhat.

2-8 Discussion

In this chapter a method has been investigated to decrease the memory and computational issues arising in retrieving the Transmission Matrix (TM) from high resolution intensity measurements alone. The proposed method decomposes the input and output fields into finite and complete basis set of guided LP modes, and the TM forms a mapping between the modal coefficients as opposed to individual pixels. The benefits of this approach is firstly a decreases of the phase retrieval problem dimensionality. The number of unknowns is decreased significantly from N^2M^2 to n_{max} , where N and M are the number of SLM and camera pixels respectively and n_{max} is the number of guided fibre modes which is orders of magnitude lower than N^2M^2 . This implicates that the number of computations needed, compared to the traditional TM formulation, is reduced from M^2 to 1 (arguably a more).

Secondly the method is much more memory efficient since the transverse mode fields are

stored compressively. However this compression method restricts the choice of phase retrieval solvers to alternating projection style algorithms as this is the only algorithm capable of handling the compressive storage of the modes.

A third gain is a decrease in the number of required measurements. In stead of N^2 measurements theoretically only a single measurement will do to obtain the 'modal' TM. More measurements will produce more accurate estimates, especially in noisy conditions.

These improvements all come at the cost of extra computations. The chosen basis of the guided transverse fibre modes is a complete set, in the sense that it spans the solution space. However compression and decompression is not very computationally efficient and have to be performed twice per iteration in the alternating projection algorithm. For that reason the modal basis expansion does decrease the dimensionality of the problem but is still relatively slow for implementation on real fibres with spatially varying transmission characteristics.

Computer simulations are conducted with a special class of MMFs, the few-mode fibres, in this case only 18 guided modes are available. The running times of popular phase retrieval algorithms are compared when solving the reduced dimensional problem. For imaging applications a much larger number of modes is required as to increase the imaging resolution, i.e. a higher Numerical Aperture (NA). This also imposes an important constraint to the camera sizes since Γ needs to be a 'tall' matrix, or at least square, in order to be an overdetermined system of equations. Take the fibre with $V = 138$ again as an example, which yields about 9500 accepted modes. That means that, in order to obtain a square Γ matrix, also 9500 camera pixels are required. For a square grid that means (98×98) pixels. For more accurate reconstruction, especially if measurements are noisy, it is desired to increase the number of camera pixels.

In summary, the only algorithm capable of solving the large scale phase retrieval problem of Eq. (2-35), and on an ordinary consumer computer, is the compressed Gerchberg-Saxton algorithm. However, the computational time still remains an issue for application on a real setup.

Chapter 3

Point Spread Function Identification

Up until now, the fibre's transmission characteristics were modelled as a mapping between Spatial Light Modulator (SLM) surface field and camera intensities. Modal decomposition lowers the computational burden but nevertheless resulted in dealing with very large matrices. Avoiding the usage of interferometric methods results in having to solve the notorious phase retrieval problem which, due to the dimensionality, has been shown to be impractical at this time. Especially, in a setting where the optical fibre is allowed to move thereby changing its transmission characteristics, it demands a more rapid identification method of the transmission model. In this chapter a different approach is proposed where the fibre is modelled by its Point Spread Function (PSF).

3-1 Model

In the following approach the optical fibre is modelled by its coherent PSF such that the output image becomes a convolution of the input image with the fibre's PSF as follows:

$$y_k = d * x_k + w_k \quad (3-1)$$

where $x_k \in \mathbb{C}^{N \times N}$, $y_k \in \mathbb{C}^{N \times N}$ and $w_k \in \mathbb{C}^{N \times N}$ are the input field, output field and Gaussian acquisition noise respectively. d is the fibre's coherent PSF and '*' represents the (2 dimensional) convolution operation:

$$d[i, j] * x_k[i, j] = \sum_{n_1=-\infty}^{\infty} \sum_{n_2=-\infty}^{\infty} d[n_1, n_2] x_k[i - n_1, j - n_2] \quad (3-2)$$

where i and j are the spatial coordinates of the image pixels.

Using the convolution theorem Eq. (3-1) can be turned into a point-wise multiplication, denoted by ' \odot ', in the frequency domain, giving

$$Y_k = D \odot X_k + W_k \quad (3-3)$$

where $Y_k = \mathcal{F}\{y_k\}$, $X_k = \mathcal{F}\{x_k\}$, $D = \mathcal{F}\{d\}$ and $W_k = \mathcal{F}\{w_k\}$ are the discrete Fourier transformations of respectively y_k , x_k , d and w_k . Suppose that the complex field y_k is measurable. In that case the fibre PSF can be obtained by simple deconvolution, performed in the Fourier domain, such that

$$\hat{d} = \mathcal{F}^{-1} \left\{ \frac{Y_k}{X_k} \right\} \quad (3-4)$$

where the division is again element-wise, and $X(k) \neq 0$. Note that in practice the images are sampled and the Fourier transform is performed numerically as a Discrete Fourier Transform (DFT). The obtained discrete frequency domain images are consequently band limited by the finite sampling frequency in the spatial domain by the Nyquist-Shannon theorem. The effects of sampling will be treated in the discussion section at the end of this chapter.

Eq. (3-4) obviously does not take noise into account and would produce poor results. More reliable estimates can be obtained by acquiring more input output images and estimate d in a least squares sense shown in Eq. (3-5), assuming the additive noise to be zero mean circular Gaussian distributed: $w_k \in \mathcal{CN}(0, \sigma_w^2)$ such that $W_k = \mathcal{F}\{w_k\} \in \mathcal{CN}(0, \sigma_w^2)$.

$$\hat{D} = \frac{\sum_{k=1}^K X_k^* \odot Y_k}{\sum_{k=1}^K X_k^* \odot X_k} \quad (3-5)$$

where K input output images are measured and $\hat{d} = \mathcal{F}^{-1}\{\hat{D}\}$. At this point it can be interesting to compare Eq. (3-5) with phase diversity methods [46, 47]. Phase diversity is a technique to estimate aberrations in incoherent imaging systems from images of extended objects. Multiple images are acquired where deliberately known phase aberrations are added to the pupil function. There is a known 'diversity' between the measured images, hence the name 'phase diversity', which provides the information to uniquely recover the systems PSF and object. However, phase diversity methods are predominantly used in *incoherent* imaging systems because of its inherent 'linearity in intensity'. The image intensity y_k for incoherent and coherent illumination is given as follows

$$\text{Incoherent} \quad |y_k|^2 = |d|^2 * |x_k|^2 \quad (3-6)$$

$$\text{Coherent} \quad |y_k|^2 = |d * x_k|^2 \quad (3-7)$$

This shows why phase diversity, and deconvolution methods, are well suited for incoherent imaging systems since $|d|^2$ can be obtained from intensity measurements only. In the coherent case there appears again the familiar nonlinearity. The implication to Eq. (3-5) now becomes clear as Y_k is unknown since:

$$Y_k = \mathcal{F}\{d * x_k\} \neq \mathcal{F}\{|d * x_k|\} \quad (3-8)$$

The Fourier transform of the intensity $|y_k|^2$ is, for coherent imaging, in fact the autocorrelation of its spectrum [48]:

$$\mathcal{F}\{|y_k|^2\} = (D \odot X_k) \star (D \odot X_k) \quad (3-9)$$

$$= Y_k \star Y_k \quad (3-10)$$

where ' \star ' represents the autocorrelation operation defined as:

$$Y_k[u, v] \star Y_k[u, v] = \sum_{n_1=-\infty}^{\infty} \sum_{n_2=-\infty}^{\infty} Y_k[n_1, n_2] Y_k^*[n_1 - u, n_2 - v] \quad (3-11)$$

where u and v are the spatial frequency components.

It is therefore proposed to solve Eq. (3-5) iteratively via alternating projections between constrained sets of y_k and d or equivalently Y_k and D . This proposed approach can thus be viewed as a coherent version of multiframe phase diversity or blind deconvolution methods.

3-2 Relation to Transmission Matrix approach

The convolution perspective, as introduced in the previous section, seems as a totally different viewpoint to the problem, but is in fact closely related to the Transmission Matrix (TM) approach discussed in Chapter 2. The TM approach can be viewed as convolution written as a matrix vector product, where the TM is the convolution matrix. Vice versa the convolution method can be transformed to a matrix vector product, however, here is where the properties of the Fourier transformation can be exploited. The convolution turns into an element-wise multiplication in the frequency domain, which when written as a matrix-vector product, yields a significant reduction in complexity. This is seen in Eq. (3-12) and Eq. (3-13)

$$Y_k = D \odot X_k + W_k \iff \mathbf{c}_y = \tilde{\mathbf{D}} \mathbf{c}_x + \mathbf{w} \quad (3-12)$$

where $\tilde{\mathbf{D}} = \text{diag}(D) \in \mathbb{C}^{N^2 \times N^2}$ becomes a diagonal matrix containing all the elements from D . $\mathbf{c}_y = \text{vec}(Y_k)$, $\mathbf{c}_x = \text{vec}(X_k)$ and $\mathbf{w} = \text{vec}(W_k)$ contain the columnised entries from Y_k , X_k and W_k respectively.

$$\begin{array}{|c|c|c|c|} \hline D_{11} & D_{12} & D_{13} & D_{14} \\ \hline D_{21} & D_{22} & D_{23} & D_{24} \\ \hline D_{31} & D_{32} & D_{33} & D_{34} \\ \hline D_{41} & D_{42} & D_{43} & D_{44} \\ \hline \end{array} \odot \begin{array}{|c|c|c|c|} \hline X_{11} & X_{12} & X_{13} & X_{14} \\ \hline X_{21} & X_{22} & X_{23} & X_{24} \\ \hline X_{31} & X_{32} & X_{33} & X_{34} \\ \hline X_{41} & X_{42} & X_{43} & X_{44} \\ \hline \end{array} = \begin{bmatrix} D_{11} & 0 & 0 & 0 & \cdots & 0 \\ 0 & D_{12} & 0 & 0 & \cdots & 0 \\ 0 & 0 & D_{13} & 0 & \cdots & 0 \\ 0 & 0 & 0 & D_{14} & \cdots & 0 \\ \vdots & \vdots & \vdots & \vdots & \ddots & \vdots \\ 0 & 0 & 0 & 0 & \cdots & D_{44} \end{bmatrix} \begin{bmatrix} X_{11} \\ X_{12} \\ X_{13} \\ X_{14} \\ X_{21} \\ \vdots \\ X_{44} \end{bmatrix} \quad (3-13)$$

From Eq. (3-12) and Eq. (3-13) is apparent that the TM in the frequency domain becomes a diagonal matrix. This physically means that the phase and amplitude of every spatial

frequency component of the propagating light is altered, i.e. multiplied by a complex number, and is independent of the other spatial frequencies. This decoupling effect is exploited and results in a significant reduction of the number of elements to be estimated scaling linearly with the number of camera pixels instead of quadratic.

This is essentially an equivalent strategy as proposed in Chapter 2, with the only difference being the expansion basis. In Chapter 2 a decoupled system was obtained after an expansion into the theoretical transverse modes excited in the fibre, where the modulation was a phase only term, whereas in this chapter the Fourier basis is used with generally complex modulation. A clear advantage of the latter method is the availability of the very efficient numerical implementation of the discrete Fourier transform in the FFT algorithm. This accounts for most of the speed increase with respect to mode-based method from Chapter 2.

3-3 Alternating projections

The fibre's PSF is found by an alternating projection-style algorithm, similar to the phase retrieval problem in Chapter 2, to account for the unknown phase of y_k . The algorithm requires a number of measured input-output image frames, where the input fields x_k for $k = 1, \dots, K$ are randomly generated with the SLM to be persistently exiting, or as diverse as possible, as will be elaborated further on. The algorithm consists of the following steps shown in Table 3-1 and is schematically depicted in Figure 3-1.

Table 3-1: Multiframe deconvolution by alternating projections

Required	$x_k, y_k k = 1, 2, \dots, K, i_{max}$	
Initialise	θ_k such that $y_k = y_k e^{j\theta_k}$	
	$X_k = \mathcal{F}(x_k)$ and $Y_k = \mathcal{F}(y_k)$	
repeat		
1. $\hat{D} \leftarrow \frac{\sum X_k^* \odot \hat{Y}_k}{\sum X_k^* \odot X_k}$	Estimate \hat{D} from Eq. (3-5)	
2. $ \hat{D} \leftarrow D $	Impose magnitude constraint on \hat{D}	
for $k = 1, 2, \dots, K$		
3. $\hat{Y}_k \leftarrow \hat{D} \odot X_k$	Compute \hat{Y}_k based on \hat{D}	
4. $ \mathcal{F}^{-1}(\hat{Y}_k) \leftarrow y_k $	Impose magnitude constraint on $\mathcal{F}^{-1}(\hat{Y}_k)$	
5. $i \leftarrow i + 1$		
untill	$i > i_{max}$	

In Table 3-1 the projections alternate between the constraint sets of y_k and d , but could equivalently be between Y_k and D . In this case the constraint set $\mathbb{Y} = \{Y_k \in \mathbb{C} : |\mathcal{F}^{-1}(Y_k)| = |y_k|\}$ where $|y_k|$ is the square root of the measured intensity, is nonconvex which means the algorithm is prone to converge to local optima.

3-4 Computing the SLM phases

Having an estimated PSF of the fibre the goal now is to find the Spatial Light Modulator (SLM) phase pattern x_d that would produce a sharp focal spot in the target plane. However

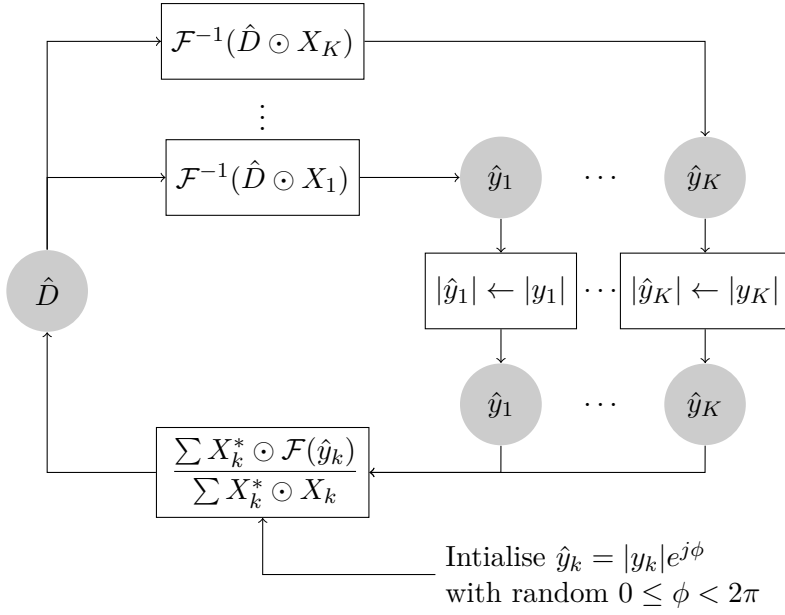


Figure 3-1: Schematic representation of the multiframe alternating projection algorithm for K frames

most SLM's are phase-only modulators having no control over the amplitude of the input field, i.e. $|x_d| = 1$. The desired intensity pattern is specified in the spatial domain denoted as $|y_d|^2$. Note that only the magnitude/intensity is of interest and the phase is not and is allowed to be arbitrary. Computing the input field x_d that would produce $|y_d|^2$ is done as follows.

$$x_d = \mathcal{F}^{-1} \left\{ \frac{Y_d}{\hat{D}} \right\} \quad (3-14)$$

where $Y_d = \mathcal{F}\{|y_d|\}$ and $\hat{D} = \mathcal{F}\{\hat{d}\}$. From Eq. (3-14) arise two issues. First issue is that in this scenario x_d will not have unit magnitude in general, and a phase-only SLM would not be able to produce the required x_d . Secondly Y_d is the Fourier transform of a magnitude only signal, so with a *flat* phase profile, which is not exactly required. But the computed input x_d is the optimal solution for this flat phase profile.

So in summary we have to solve the dual problem of Eq. (3-1); find the input phase $x \in \mathbb{C} : |x| = 1$ given the PSF d and desired output $|y|$. This could be solved iteratively again by alternating projections, however now there is only a single frame available. The lack of additional image frames is detrimental to the performance of the multiframe deconvolutions algorithm as will be shown in the next sections. The lack of information from additional image frames in fact divert the input away from a sensible solution. The applied input x_d is therefore the phase-only constrained solution from Eq. (3-14). This is essentially a single iteration of the single-frame alternating projection algorithm. Hence the computed input phase is in fact suboptimal.

3-5 Experiments

In section the performance of the algorithm is studied in computer simulations. In the experiment is evaluated how the PSF formulation, in combination with the multiframe deconvolution algorithm, performs when used to form a sharp focus a small distance behind the distal fibre tip. An image of the SLM surface is formed onto the surface of the optical fibre as shown in Figure 3-2, where the goal is to find the required SLM phases such that a sharp focus is formed at the target plane as a result of constructive interference. The light propagation through the Multi Mode Fibre (MMF) is simulated numerically, where material impurities are considered as random changes of the refractive index profile of the fibre. For details and implementation of the fibre simulator please consult Appendix B.

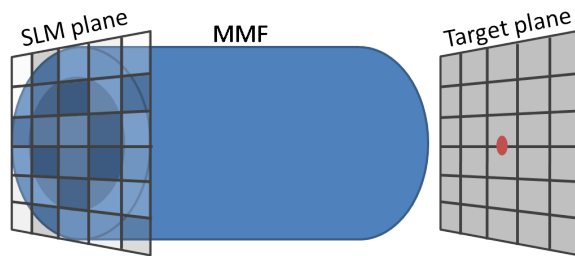


Figure 3-2: Experimental setup where the 'SLM plane' is conjugated to the SLM surface and the 'target plane' to the CCD camera. Proper SLM settings would yield constructive interference at the specified location in the target plane

For the experiment a number of 512×512 SLM phase patterns are randomly generated which are then propagated numerically through the optical fibre where their resulting intensity images are recorded. These input-output pairs are then used in the multiframe deconvolution algorithm to compute an estimate of the fibre's PSF. Finally a focus is formed at the fibre output by inverting the estimated model as explained in the previous section, essentially feed-forward control, and the 'quality' of this focus is evaluated in terms of squared euclidean distance between measured and target intensity images: $\sum(|y_d|^2 - |y|^2)^2$. The target intensity pattern $|y_d|^2$ is defined as a single pixel in the middle of the image frame with unit intensity, and $|y|^2$ is the measured intensity image after the identification cycle and is normalised to have unit intensity. In the experiment the effect of the number of iterations and image frames on the imaging performance and computational time is evaluated, as well as the effect of diversity of the SLM phase pattern. Disturbances acting on the fibre are not taken into consideration as to simulate a rigid fibre with constant propagation properties over the duration of experiment.

3-6 Results

First the performance of the multiframe deconvolution algorithm is evaluated for different numbers of iteration and measured image frames. The obtained PSF is used for imaging and the quality of the focus is evaluated according to the squared euclidean distance between the measured and target intensity. Also the computing time of the algorithm was measured. The experiment is repeated 10 times and results are averaged and normalised giving the result in Figure 3-3.

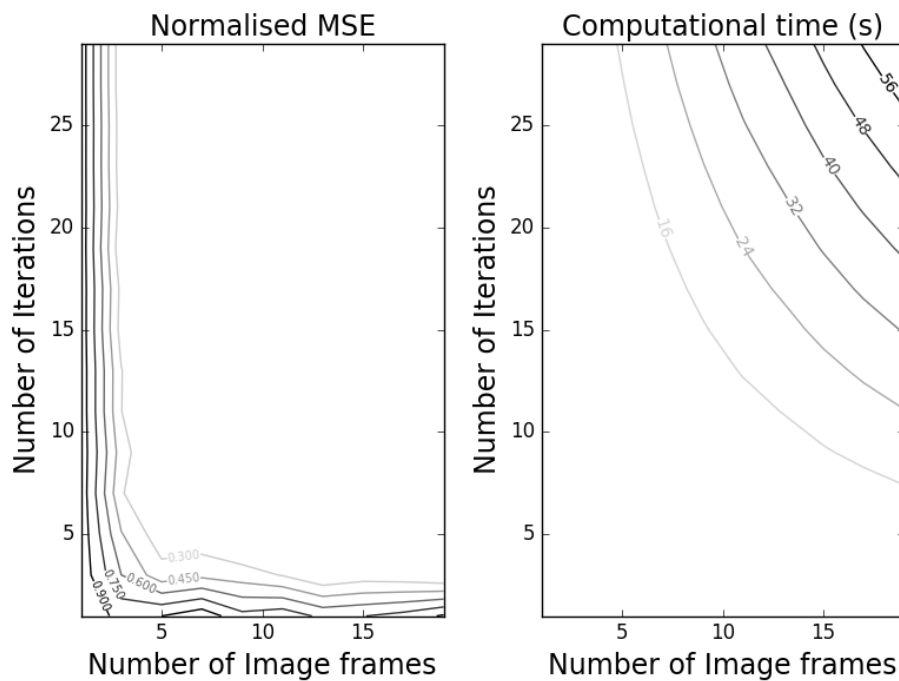


Figure 3-3: Normalised MSE (left), and running times in seconds (right) of the multiframe deconvolution algorithm for various number of iterations and image frames

Secondly the effect of the (lack of) diversity of the input phase pattern, generated by the SLM, on the identification process is investigated. The input should excite the system in the most optimal way to extract most information about the system as possible. The input phases are randomly drawn from a zero mean Gaussian distribution with varying standard deviation σ_x , to control the diversity of the input field. A small standard deviation results in less phase variation within one input frame, and therefore also variety within the set of image frames. For this simulation the set of image frames used for the identification is set to 10 and the number of iterations is 10. The multiframe deconvolution algorithm estimates the fibre's PSF for different sets of input frames all having a different input standard deviation. The obtained PSF is used to form a sharp focal spot again at the target plane and is compared with the target. The experiment is repeated 25 times and results are averaged giving the results in Figure 3-4

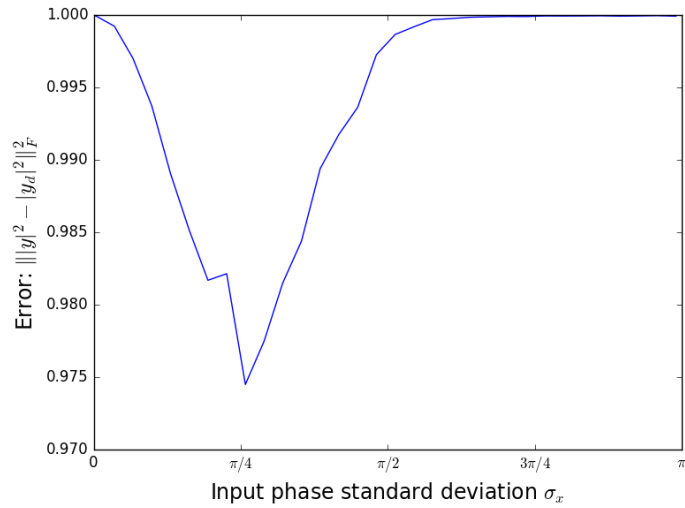


Figure 3-4: Imaging performance, measured as squared euclidean distance between output and target, as a function of input phase standard deviation

It can be seen in Figure 3-4 that input phase patterns with little diversity yield poor performance, as expected. The system is not excited persistently enough to provide sufficient information for the identification process. However there is a clear optimum around $\sigma_x = \pi/4$ since too much diversity shows to have an adverse effect as well. The reasons for this are discussed further on in the discussion section.

3-6-1 Demonstration of the principle

As an illustrative example the target intensity pattern is set to be the prometheus flame of the TU Delft logo. After estimating the fibre's PSF, with 10 input-output image frames, and 10 iterations, an input phase pattern from a 512×512 SLM grid is computed. The SLM surface is projected onto the fibre's surface in the numerical fibre propagation simulator and the output intensity is compared to the intensity obtained from the PSF model. The results are shown in Figure 3-5.

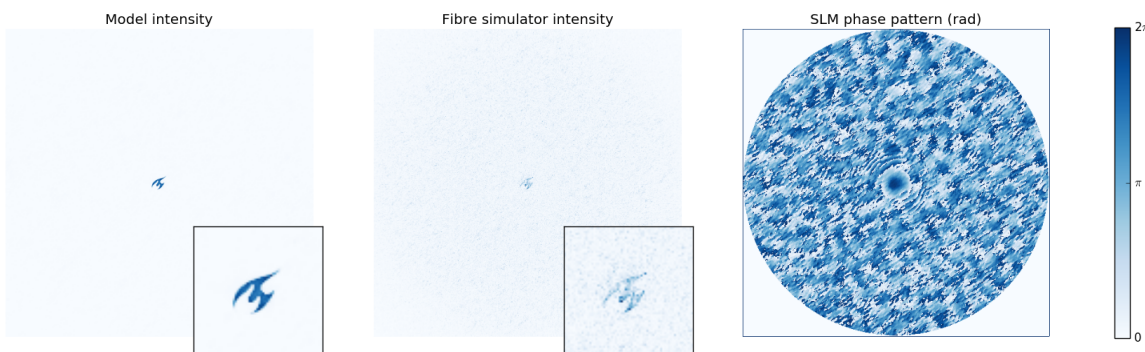


Figure 3-5: Output intensity from the identified PSF (left) and the output intensity from the fibre propagation simulation (middle) after the input phase pattern (right) is given as an input.

To have maximal control over the field entering the fibre, it's inevitable that the corner pixels will be unused as light stemming from those areas will not propagate through the fibre and have no influence on the output intensity. The light from those pixels is blocked such that it does not interfere with the light exiting the fibre and distort the output image. The effective number of SLM pixels contributing to the output image is thus lower. It is seen in Figure 3-5 that the image from the simulated fibre is less sharp than the PSF model predicts. The background speckle is much more prominent reducing contrast in the image.

In Figure 3-6 the same experiment is repeated but now with a target set as a single pixel with unit intensity. Now the result is from the fibre propagation simulator is much better as a near perfect spot is produced with very low background speckle. A larger size target intensity pattern, such as the TU Delft flame, naturally comprises of multiple pixels over which the energy has to be distributed, resulting in lower SNR (signal to noise ratio) and contrast.

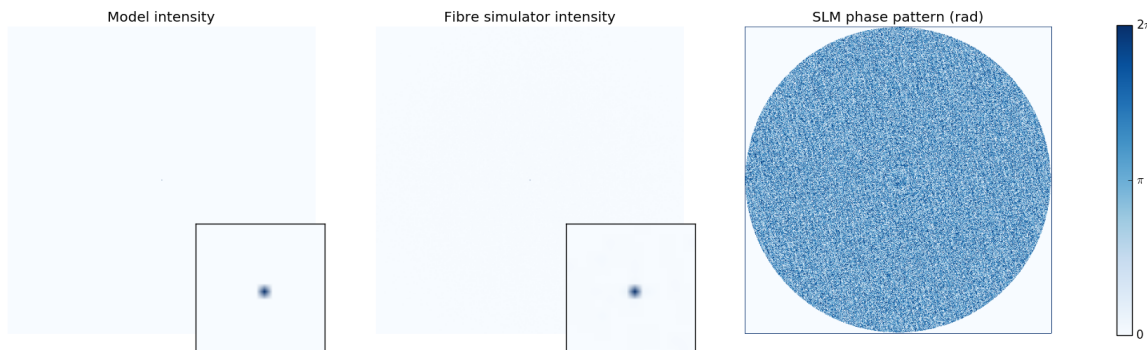


Figure 3-6: Output intensity from the identified PSF (left) and the output intensity from the fibre propagation simulation (middle) after the input phase pattern (right) is given as an input.

3-6-2 Test on laboratory setup

The multiframe deconvolution algorithm is also tested to estimate the PSF of a multimode optical fibre on a hardware setup in the optics lab. Experimentation on a real life system is still in an early phase at the time of writing and needs more tuning. It is nevertheless possible to demonstrate the principle. The fibre used has a $50\mu\text{m}$ diameter and an NA of 0.22 and supports therefore in the order of 20000 modes. For the identification the SLM uses 512×512 pixels with randomly generated phase screens, Gaussian filtered with spatial bandwidth of 51.2 pixels to control the input diversity. The detection system consists of a Leica $10\times$ microscope objective a $f = 150\text{mm}$ lens and a CMOS camera with $5.86\mu\text{m}$ sized pixels. The algorithm runs with 16 image frames and 20 iterations and an effective grid of 128×128 . The results are shown in Figure 3-7.

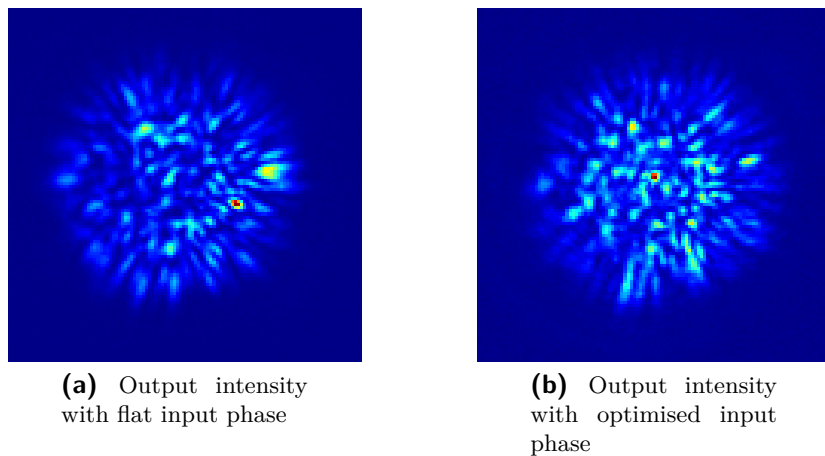


Figure 3-7: Output intensity patterns measured (a): with flat input phase and (b): with optimised phase pattern obtained using the multiframe deconvolution algorithm

It is seen that after the fibre's PSF has been identified, with the multiframe deconvolution algorithm, and an input phase pattern has been computed by model inversion as explained section 3-4, a focus is formed at the output of the fibre. However there is still a strong unwanted background speckle visible. Nevertheless is this result promising and needs careful tuning.

3-7 Discussion

3-7-1 Iterations and image frames

From Figure 3-3 can be seen that the MSE rapidly decreases with increasing number of iterations and measured image frames. From the figure, accurate estimation and imaging results are obtained by taking at least 5 input-output image frames are required with a minimum of 8 iterations. However, convergence to the global optimum is not guaranteed, and convergence to 'bad' local optima will yield unwanted results. The number of image frames is also quite low considering the random generation of the SLM phase patterns. Too much

similarity in the inputs will obviously influence the performance negatively. This is what probably causes the bulge in the '0.15'-level line in left plot of Figure 3-3. It is therefore advisable to stay on a safer side and increase the number of measured image frames and iterations. The increase comes obviously at the cost of extra computational time which is also shown in the right image in Figure 3-3. It seems that the running time of the algorithm is influenced by the number of iterations and image frames in roughly the same way. Perhaps that the cost of taking extra images is slightly higher in terms of running time. From a practical perspective is definitely desired to keep the number measurements to a minimum. This to avoid any fibre movements in between measurements. In the simulation the fibre is perfectly rigid as is hardly ever the case in practise. So the minimum of 5 images should be seen as optimistic.

3-7-2 Input diversity

As is shown in Figure 3-4, the performance of the identification method increases with input diversity up to a certain point. From that moment on the performance seemingly deteriorates. This is probably caused by the difference in spatial cut-off frequencies between the fibre and input phase profile. The spatial cut-off frequency of the fibre f_v is determined by the V-number which depends on the refractive indices of the core and cladding material, the aperture and the wavelength. The cut-off frequency of the SLM f_ϕ is determined by the pixel grid and the sampling theorem. Suppose $f_\phi > f_v$. In the case of a high σ_x , a large input diversity, the input will predominantly contain high spatial frequencies which are low-pass filtered by the fibre. Hence their arises a discrepancy between given inputs and the content of that input that contributes to the output intensity. The distinctiveness of the input frames is in the high frequency range, which is filtered out by the fibre resulting in very similar output images. In the case that $f_\phi < f_v$ all spatial frequencies generated by the SLM are supported by the fibre and contribute to the output intensity. However, there might be a range where the input is dominated too much by high spatial frequencies such that the low frequency fibre characteristics are difficult to extract. In practical situations this becomes more of a problem due to additional high frequency noise on the measurements.

3-7-3 Effect of sampling

As mentioned before, the deconvolution method is performed numerically in the Fourier domain where the finite sampling intervals and support length limit the accuracy of the method. The finite pixel size of the SLM determines the maximal spatial frequency that can be generated according to the Nyquist-Shannon theorem: $f_{max} = \frac{1}{2\Delta x}$ where Δx is the pixel size of the SLM. Consequently the frequency spacing in the Fourier domain is $\Delta f = \frac{1}{N\Delta x} = \frac{1}{L}$ where L is the support length in real space of the SLM. Δf can be seen as the resolution of the spectrum that is limited by the physical size of the SLM surface. Consequently a larger SLM surface will result in higher spectral resolution. The number of samples in the frequency domain can be increased as well by padding the spatial signal with zeros. This does not affect the spectral resolution nor the cut-off frequency but can be viewed as an interpolation in the spectral domain.

Figure 3-8 shows the curve from Figure 3-4 with the addition of simulations with half and double the SLM support size. The amount of pixels are kept the same. It shows a similar

trend but a larger support length results in the smallest error. This is expected as a small support length yields a coarse spectral resolution. The range of achievable spatial frequencies remains the same since the sampling frequency was kept constant, but most frequencies could not be represented in the Fourier domain due to the poor resolution. The cutt-off frequency is kept the same and the optimal input diversity is therefore the same for all support lengths.

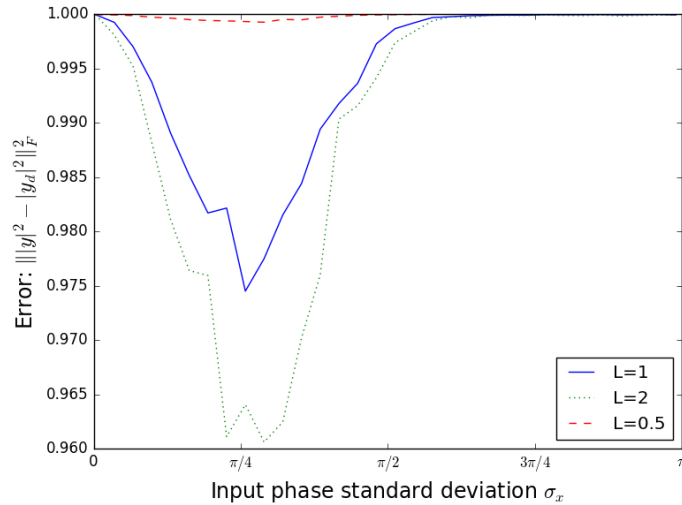


Figure 3-8: Imaging performance, measured as squared euclidean distance between output and target, as a function of input phase standard deviation for three different SLM support lengths

3-7-4 Speed of the algorithm

Finally, to illustrate the speed of the multiframe deconvolution algorithm, the fibre PSF is calculated for different grid sizes and plotted compared to the modal decomposition method of Chapter 2. Although this is not a completely fair comparison it is nonetheless illustrative.

Where in Chapter 2 the transverse fibre modes were used as an expansion basis in this chapter the Fourier basis is used which can rely on the fast FFT algorithm. It was shown that the modal decomposition method decreases the computational load but that the chosen expansion basis was computationally quite demanding.

To recall, in Chapter 2 the following phase retrieval problem was solved for different camera pixel grid sizes M

$$\mathbf{y} = |\boldsymbol{\Gamma}\boldsymbol{\alpha}|^2 \quad (3-15)$$

with $\mathbf{y} \in \mathbb{R}^{M^2}$ and $\boldsymbol{\alpha} \in \mathbb{C}^{18}$. Hence the number of modes were kept constant and set to 18. Note that this is not a very realistic example, but was intentionally kept low to avoid memory errors. The multiframe deconvolution algorithm uses not only multiple measurements but also requires equal and square grids of input and output fields. This implicates that the number of (Fourier) modes is M^2 as opposed to 18. This is where the comparison is flawed. Eventhough the multiframe deconvolution algorithm solves a much higher dimensional problem, it still

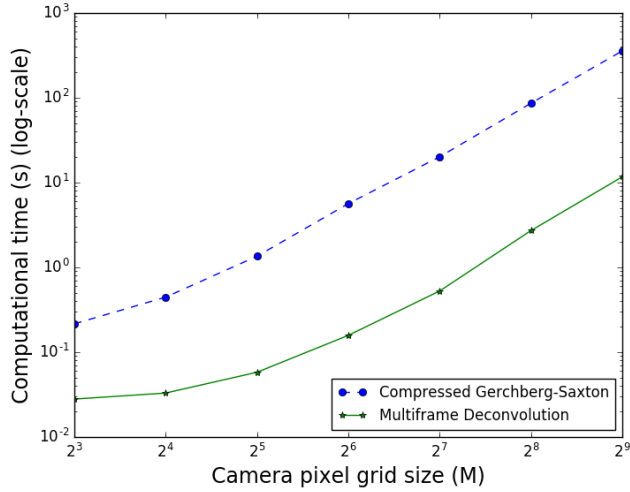


Figure 3-9: Demonstration of the speed of the multiframe deconvolution algorithm compared to the modal decomposition method of Chapter 2 solved by alternating projections, for different grid sizes.

outperforms the fibre modes based method from Chapter 2 as is shown in Figure 3-9. The FFT algorithm accounts for most of this speed increase.

Chapter 4

Control

During the identification process and in operation, the fibre's transmission characteristics are ought to be constant. Therefore the fibre should be held as rigid as possible during the identification process as the transmission properties greatly depend on the bending state of fibre. As a consequence the transmission model of only that single orientation is obtained, and only that orientation can be used for operations. Especially in the feed-forward control method, as proposed in previous sections, model mismatches are detrimental to the imaging performance. In most practical applications it is preferable to exploit the fibre's flexible nature and use it in a range of configurations. Proposals in literature to tackle this problem predominantly focus on fast recalculation of the Transmission Matrix (TM) online, with fast algorithm implementations [49] and on GPUs [50], or faster optimisation algorithms [13, 2]. Also switching between measured TMs for a number of predefined configurations is proposed in [51]. Speed increase is also achieved by substituting a Digital Micromirror Device (DMD) for an Spatial Light Modulator (SLM) [27, 52] and the usage of interferometric methods to access the complex field of the camera measurements to avoid the phase retrieval problem. The multiframe deconvolution algorithm proposed in the previous chapter shows to be a relatively quick identification method, so in this chapter an attempt is made to close the loop by designing an Iterative Learning Control (ILC) strategy to compensate for small fibre perturbations, and its potential is demonstrated in computer simulations.

4-1 Rolling window

A straight forward way to update the model is by letting the identification algorithm run while in operation and add the new input-output frames to the data set, while discarding old measurements. This configuration is shown in a block scheme in Figure 4-1.

This online identification approach suffers from the lack of diversity in the input images x as \hat{D} gets close to D . For accurate identification of the fibre's Point Spread Function (PSF), the set of used input fields should be as diverse as possible, while in closed loop operation the computed inputs $x(t)$ will become too similar, with no additional information gain. These

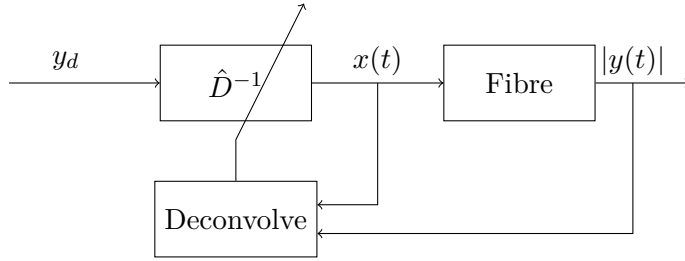


Figure 4-1: Block scheme of online identification method with a rolling window

very similar inputs will at some point fill the rolling window completely, resulting in wrong PSF estimates.

4-2 Iterative Learning Control

Iterative Learning Control (ILC) is a control strategy, often used in systems that perform the same task repetitively, to compensate for tracking errors. The idea is to update the control input iteratively based on knowledge of previous trial inputs, the tracking error and a model of the system. When an exact model of the system is available, clearly the optimal control input to track a specified reference is obtained by inverting this model, which is considered as feed-forward control. Obviously when the model is not completely known, perfect tracking will never be achieved. ILC is an iterative search method that converges to the optimal control input signal that minimises the tracking error. It can therefore be seen as a "feedback system in the trial domain, and a feed-forward system in the time domain" [53]. With a model available from the identification procedure in Chapter 3, which is not strictly required for ILC, the proposed control method is very similar to Newton's root finding method as will be shown in the following section.

4-3 Model

Recapitulating, we assume the following relation between the input field $x(t)$ generated by the SLM and output field $y(t)$ measured by the camera at time instant t , where d is the fibre's PSF.

$$y(t) = d * x(t) \quad (4-1)$$

From the convolution theorem follows the linear relation between input and output spectra

$$Y(t) = D \odot X(t) \quad (4-2)$$

where $Y(t) = \mathcal{F}\{y(t)\}$ and $X(t) = \mathcal{F}\{x(t)\}$ are the (discrete) Fourier transformed input and output fields, $D = \mathcal{F}\{d\}$ is the Optical Transfer Function (OTF) and ' \odot ' denotes again element wise multiplication.

Now in a more realistic environment, the acquired data for the identification process will be most likely be influenced by small disturbances and noise which will result in estimated OTF, say \hat{D} , where $\hat{D} \neq D$. Also during operation small changes in transmission characteristics will deteriorate the systems performance, since there is no feedback compensation. However it can be expected that the model mismatch from the identification is 'small enough', for application of newton method based ILC, since the multiframe deconvolution method is relatively fast. The ILC update scheme can than iteratively find the optimal control input in the case of small model errors, or after a change in spatial configuration.

The ILC update scheme in the spectral domain is given in Eq. (4-3)

$$X(t+1) = X(t) + K \frac{Y_d - Y(t)}{\hat{D}} \quad (4-3)$$

where the next control input $X(k+1)$ is updated based on the previous input $X(k)$ and the error between desired and measured output spectra $Y_d - Y(t)$, and the estimated model \hat{D} . The gain K determines the step size of the update. The update is presented in the Fourier domain to profit from the linearity and to illustrate the concept. The convergence to an optimal control input based on Eq. (4-3) is schematically shown in Figure 4-2 for step size $K = 1$.

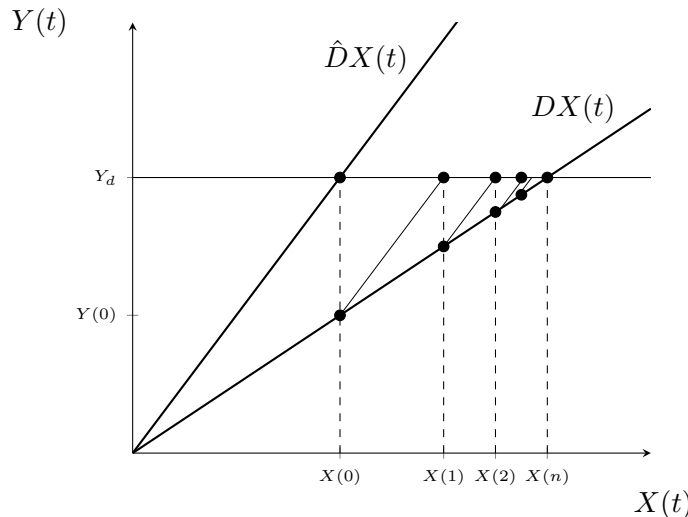


Figure 4-2: Schematic of the convergence of ILC towards the desired output Y_d by updating the input signal $X(t)$

From Figure 4-2 becomes clear that \hat{D} should be close enough to D or should at least point into the right direction to converge to the optimum. Hence big model mismatch will not result in a convergent algorithm.

4-3-1 Discussion

The apparent weak spot of the spectral ILC formulation from Eq. (4-3) is not surprisingly the phase loss in the measurements of the output intensity as well as the undefined phase of

the desired output field. The Fourier transform of a complex signal and its magnitude alone are generally not equal. Explicitly this gives:

$$Y(t) = \mathcal{F}\{|y(t)|\} \neq \mathcal{F}\{y(t)\} \quad (4-4)$$

The error signal $E(t) = Y_d - Y(t)$ does therefore not reflect the difference between the spectra of the desired and measured complex fields, but of their magnitudes. Note that Y_d is the spectrum of the desired magnitude with constant phase profile. $E(t)$ can therefore not serve as feedback signal the for given in Eq. (4-3). A second issue is that the update law does not take input constraints into consideration, which for a phase-only SLM is: $|\mathcal{F}^{-1}\{X(t)\}| = 1$. So the update law in Eq. (4-3) is applicable in cases when the complex field could be accessed, by interferometry for example, and phase and amplitude modulator is used to generate the inputs.

The ILC methodology discussed in this chapter is not yet applicable due phase ambiguity arising from the intensity measurements and phase-only restrictions of the SLM. The design of a controller that is able to compensate for fibre movements is a crucial step in fibre optic imaging technology and is left open for future research.

Chapter 5

Conclusions

5-1 Main conclusions

The work presented in this thesis can be summarised as the search for a model-based wavefront-shaping technique, capable of handling, and profit from, the large pixel counts of state of the art spatial light modulators and cameras, by using solely intensity measurements. Interferometry is considered unwanted as it requires holographic measurements, thereby increasing the complexity of the optical system. The focus has been mainly on step index multimode fibres, but could be extended to optical waveguides in general. The outline of this report has essentially been a chronological representation of the project work.

In Chapter 2 a methodology was sought to calculate the transmission matrix of an optical fibre for a 512×512 Spatial Light Modulator (SLM) and camera grid, by only using intensity measurements. This transmission matrix approach is along the line of thinking of the research at this time, and boils down to solving a large scale phase retrieval problem. The proposed approach is a decomposition into a basis of transverse modes arising from the model of wave propagation in cylindrical symmetric wave guides. This would theoretically diagonalise and shrink the Transmission Matrix (TM) significantly, from $N^2 M^2$ elements to n_{max}^2 where N and M are the pixel grid sizes of the SLM and camera respectively, and n_{max} is the number of guided modes of the optical fibre. The TM is calculated with an alternating projection style algorithm. However due to inefficient (de)composition the simplified form has not led to reduction in computational time. The method does make it possible to solve the phase retrieval problem on this scale without memory issues as opposed to the conventional TM formulation.

Chapter 3 takes on a different starting point by modelling the fibre by its Point Spread Function (PSF) and exploit Fourier properties of convolution. This approach is in fact identical to the method in Chapter 2 where in this case the Fourier basis is used instead of the transverse fibre modes. This also resulted in a tractable diagonal TM where the size depends on the chosen sampling of the images. The PSF is estimated with an alternating projection style algorithm, taking multiple input-output frames into consideration and can be considered as

a coherent multiframe deconvolution algorithm. This method is quite fast and shows good imaging performance in simulations. The method is also demonstrated on a hardware setup and is able to form a focus at a desired location. However the background speckle is still somewhat high and more tuning is necessary.

In Chapter 4 an attempt is made to close the loop and compensate for small perturbations and model mismatches via Iterative Learning Control (ILC). It shows conceptually how a Newton method type ILC controller could iteratively find the optimal SLM input phase. The critical issue is again the phase loss in the intensity measurements, and the phase-only restriction of the SLM to which the ILC update have to be adjusted. This adaptation is left for future research.

5-2 Recommendations for future work

Control

To image with multi mode optical fibres it is of great importance to be able to compensate for the changing transmission characteristics of the fibre as a consequence of bending. ILC seems a suitable approach for small bending changes or drifts but needs to be investigated further to account for the phase ambiguity arising from the intensity measurements and phase-only restriction of the SLM. For larger bends or orientation changes this method shows to fail. Potentially a model can be identified that relates the fibre's PSF with its orientation to be able to compensate for large fibre deformations. The proposed multiframe deconvolution algorithm can be of use here as data can be generated reasonable fast, opening up the way for identification of such models. The speed of the multiframe deconvolution algorithm could also be exploited to update the PSF online, in an adaptive control methodology for example. Also the temporal dynamics of the output image can be interesting to investigate. This might provide additional information about drifts or slow fibre motion for example, usable for feedback.

Multiframe deconvolution algorithm

The multiframe deconvolution algorithm has shown its potential in a real-life experiment, however the performance needs to be improved still. Reasons for this may be the sensitivity to minor perturbations or vibrations of the fibre during the identification process. This again asks for some form of feedback control. Another noise source comes from the camera measurements. In the simulations it is assumed to be Gaussian, whereas it will be more likely to be Poisson distributed. The effect of this needs more understanding and the algorithm could be adapted accordingly.

A second issue in making this method work in practise is the choice of input phase patterns used for the identification as this shows to have big influence on the imaging performance. High SLM resolutions will quickly result in too high spatial frequency content in the input field which will be filtered out by the fibre.

Another important recommendation would be to investigate alternative ways to compute the optimal input phase given the PSF and desired output intensity pattern. Alternating

projections seems to go wrong as a single image frame provides to little information to convert to a good solution.

Appendix A

Phase Retrieval algorithms

In this chapter more detailed derivations are given for the phase retrieval algorithms discussed in Chapter 2. First PhaseLift and PhaseCut will be discussed which are both based semidefinite programming, followed by the Bayesian style, prVBEM algorithm. The derivations in this chapter are by no means complete but serve as supporting information for the main text. For more details please consult the cited literature.

Semidefinite programming

Apart from the popular Gerchberg-Saxton algorithm there are more ways to solve the phase retrieval problem. The method in this section is based on a convex relaxation. The method starts by observing that Eq. (2-35) describes a set of quadratic relations that can be rewritten as linear equations in a higher dimension. Starting from Eq. (2-35) and exploiting the trace operator:

$$y_i = |\boldsymbol{\gamma}_i \boldsymbol{\alpha}|^2 = \boldsymbol{\gamma}_i \boldsymbol{\alpha} \boldsymbol{\alpha}^H \boldsymbol{\gamma}_i^H = \text{Tr}(\boldsymbol{\gamma}_i^H \boldsymbol{\gamma}_i \boldsymbol{\alpha} \boldsymbol{\alpha}^H) = \text{Tr}(\mathbf{Y}_i \mathbf{A}) \quad (\text{A-1})$$

where $\mathbf{A} = \boldsymbol{\alpha} \boldsymbol{\alpha}^H$ and $\mathbf{Y}_i = \boldsymbol{\gamma}_i^H \boldsymbol{\gamma}_i$ with $\boldsymbol{\gamma}_i$ is the i^{th} row of $\boldsymbol{\Gamma}$. The goal is now to find \mathbf{A} that satisfies Eq. (A-1), or more formally:

$$\begin{aligned} & \text{find } \mathbf{A} \\ & \text{s.t. } y_i = \text{Tr}(\mathbf{Y}_i \mathbf{A}), i = 1, 2, \dots, M^2 \\ & \quad \mathbf{A} \succeq 0 \\ & \quad \text{Rank}(\mathbf{A}) = 1. \end{aligned} \quad (\text{A-2})$$

Eq. (A-2) is equivalent to the the following rank minimisation problem.

$$\begin{aligned} & \min \text{ Rank}(\mathbf{A}) \\ & \text{s.t. } y_i = \text{Tr}(\mathbf{Y}_i \mathbf{A}), i = 1, 2, \dots, M^2 \\ & \quad \mathbf{A} \succeq 0. \end{aligned} \quad (\text{A-3})$$

Since rank minimisation is a hard combinatorial problem the minimum rank objective is relaxed and replaced by the trace of \mathbf{A} , such that the following optimisation problem is obtained:

$$\begin{aligned} \min \quad & \text{Tr}(\mathbf{A}) \\ \text{s.t.} \quad & y_i = \text{Tr}(\mathcal{Y}_i \mathbf{A}), \quad i = 1, 2, \dots, M^2 \\ & \mathbf{A} \succeq 0. \end{aligned} \tag{A-4}$$

This is a convex problem for which many of-the-shelf numerical solvers exist. Eq. (A-4) is what is known as the "PhaseLift" algorithm [35, 36].

Another interesting approach, worth mentioning, is taken in [37]. The algorithm proposed, called "PhaseCut", is based on the MaxCut algorithm [41] and separates \mathbf{y} into an amplitude component and a phase component, $\boldsymbol{\Gamma}\boldsymbol{\alpha} = \text{diag}(\mathbf{y})\mathbf{u}$, where $\mathbf{u} \in \mathbb{C}^{M^2}$ is a phase vector satisfying $|u_i| = 1$. The phase retrieval can thus be written as:

$$\begin{aligned} \min_{\boldsymbol{\alpha}, \mathbf{u}} \quad & \|\boldsymbol{\Gamma}\boldsymbol{\alpha} - \text{diag}(\mathbf{y})\mathbf{u}\|_2^2 \\ \text{s.t.} \quad & |u_i| = 1, \quad i = 1, 2, \dots, M^2 \end{aligned} \tag{A-5}$$

The optimisation over $\boldsymbol{\alpha}$ is in this form a standard least squares problem and can be solved explicitly as

$$\boldsymbol{\alpha} = \boldsymbol{\Gamma}^\dagger \text{diag}(\mathbf{y})\mathbf{u} \tag{A-6}$$

Substituting this into Eq. (A-5) gives:

$$\begin{aligned} \min_{\boldsymbol{\alpha}, \mathbf{u}} \quad & \|\boldsymbol{\Gamma}\boldsymbol{\Gamma}^\dagger \text{diag}(\mathbf{y})\mathbf{u} - \text{diag}(\mathbf{y})\mathbf{u}\|_2^2 \\ \text{s.t.} \quad & |u_i| = 1, \quad i = 1, 2, \dots, M^2 \end{aligned} \tag{A-7}$$

Rewriting the objective as

$$\|\boldsymbol{\Gamma}\boldsymbol{\Gamma}^\dagger \text{diag}(\mathbf{y})\mathbf{u} - \text{diag}(\mathbf{y})\mathbf{u}\|_2^2 = \mathbf{u}^H \text{diag}(\mathbf{y}^T)(\mathbf{I} - \boldsymbol{\Gamma}\boldsymbol{\Gamma}^\dagger)\text{diag}(\mathbf{y})\mathbf{u} \tag{A-8}$$

the phase retrieval problem now becomes

$$\begin{aligned} \min_{\mathbf{u}} \quad & \mathbf{u}^H \mathbf{M} \mathbf{u} \\ \text{s.t.} \quad & |u_i| = 1, \quad i = 1, 2, \dots, M^2 \end{aligned} \tag{A-9}$$

Where $\mathbf{M} = \text{diag}(\mathbf{y}^T)(\mathbf{I} - \boldsymbol{\Gamma}\boldsymbol{\Gamma}^\dagger)\text{diag}(\mathbf{y})$ is a Hermitian positive semidefinite matrix. Defining $\mathbf{U} = \mathbf{u}^H \mathbf{u}$, the quadratic program in Eq. (A-9) can be also written as a semidefinite programming problem as

$$\begin{aligned}
\min \quad & \text{Tr}(\mathbf{U}\mathbf{M}) \\
\text{s.t.} \quad & \text{diag}(\mathbf{U}) = 1 \\
& \mathbf{U} \succeq 0 \\
& \text{rank}(\mathbf{U}) = 1.
\end{aligned} \tag{A-10}$$

Eq. (A-10) is known as the MaxCut algorithm [41]. For the phase retrieval problem the nonconvex rank constraint is dropped to finally obtain the convex optimisation problem

$$\begin{aligned}
\min \quad & \text{Tr}(\mathbf{U}\mathbf{M}) \\
\text{s.t.} \quad & \text{diag}(\mathbf{U}) = 1 \\
& \mathbf{U} \succeq 0
\end{aligned} \tag{A-11}$$

As becomes evident from the derivations above is that solving the already large dimensional phase retrieval problem in higher dimensions via semidefinite programming, increases the computational burden even more. In addition, there is no guarantee that minimising the rank will yield a rank-1 matrix even if there is a unique solution.

Bayesian estimation

The nonlinearity of the modulus can be circumvented by a Bayesian point of view, first proposed in [24]. In this paper the focus is on compressive sensing where the underlying signal, $\boldsymbol{\alpha}$ in this case, is assumed to be sparse. The algorithm is based on 'loopy belief propagation', and in particular the "Generalised Approximate Message Passing" (GAMP) algorithm from [42]. Shortly after, in [38], phase retrieval for a full non-sparse signal was proposed by following a Bayesian variational approach based on a mean field approximation, called phase retrieval Variational Bayesian Expectation Maximisation (prVBEM). In [27] a Transmission Matrix (TM) of size 900 by 40000 was estimated with the this algorithm.

In this thesis the workings of the prVBEM algorithm is discussed as this algorithm is suited for estimation of dense (non-sparse) vectors and shows good performance in terms of accuracy and computational complexity [27].

Eq. (2-35) is reinterpreted in the Bayesian approach where the missing phase in the measurement vector is introduces as a new variable. Every absolute valued (pixel) measurement y_μ , $\mu = 1, 2, \dots, M^2$ is thus modelled as

$$y_\mu = e^{j\theta_\mu} \left(\sum_{i=1}^{N^2} \gamma_{\mu,i} \alpha_i + n_\mu \right) \tag{A-12}$$

The missing phase is denoted by $\theta_\mu \in [0, 2\pi)$ and n_μ is a zero-mean circular Gaussian noise with variance σ_n^2 . Note that the subscript μ is used, as opposed to j in previous notation, to distinguish it from the complex $j = \sqrt{-1}$. $\gamma_{\mu,i}$ is the i^{th} element in the μ^{th} row of $\boldsymbol{\Gamma}$ and $\boldsymbol{\alpha}_i$ is the i^{th} element of $\boldsymbol{\alpha}$

In the Bayesian approach the signals are assumed to be realisations of random variables. The probability densities corresponding to the variables are supposed to be

$$p(\boldsymbol{\alpha}) = \prod_{i=1}^{N^2} p(\alpha_i) \quad \text{with} \quad p(\alpha_i) = \mathcal{CN}(0, \sigma_\alpha^2) \quad (\text{A-13})$$

$$p(\boldsymbol{\theta}) = \prod_{\mu=1}^{M^2} p(\theta_\mu) \quad \text{with} \quad p(\theta_\mu) = \frac{1}{2\pi} \quad (\text{A-14})$$

The goal is again to recover the complex signal $\boldsymbol{\alpha}$ and can be defined as the solution to the marginalised Maximum A Posteriori (MAP) estimation:

$$\hat{\boldsymbol{\alpha}} = \operatorname{argmax}_{\boldsymbol{\alpha}} p(\boldsymbol{\alpha}|\mathbf{y}) \quad (\text{A-15})$$

with

$$p(\boldsymbol{\alpha}|\mathbf{y}) = \int_{\boldsymbol{\theta}} p(\boldsymbol{\alpha}, \boldsymbol{\theta}|\mathbf{y}) \quad (\text{A-16})$$

However due to the marginalisation of $\boldsymbol{\theta}$ the computation of $p(\boldsymbol{\alpha}|\mathbf{y})$ is intractable. Variational methods are a number of techniques to approximate intractable integrals such as in Eq. (A-16). In [38] the mean field approximation, a specific of variational method, is proposed to approximate $p(\boldsymbol{\alpha}, \boldsymbol{\theta}|\mathbf{y})$ by $\hat{q}(\boldsymbol{\alpha}, \boldsymbol{\theta})$, which is a much simpler distribution function. The lack of similarity between the approximation $\hat{q}(\boldsymbol{\alpha}, \boldsymbol{\theta})$ and the real joint distribution $p(\boldsymbol{\alpha}, \boldsymbol{\theta}|\mathbf{y})$ is measured by a dissimilarity function, which for the mean field approximation is the Kullback-Leibler (KL) divergence condition, defined as

$$d_{KL}(q\|p) = \int_{\boldsymbol{\alpha}} \int_{\boldsymbol{\theta}} q(\boldsymbol{\alpha}, \boldsymbol{\theta}) \log\left(\frac{q(\boldsymbol{\alpha}, \boldsymbol{\theta})}{p(\boldsymbol{\alpha}, \boldsymbol{\theta}|\mathbf{y})}\right) d\boldsymbol{\alpha} d\boldsymbol{\theta} \quad (\text{A-17})$$

Therefore the best approximation is the one minimising the KL divergence condition:

$$\hat{q}(\boldsymbol{\alpha}, \boldsymbol{\theta}) = \operatorname{argmin}_{q \in \mathcal{F}} d_{KL}(q\|p) \quad (\text{A-18})$$

where $\hat{q}(\boldsymbol{\alpha}, \boldsymbol{\theta})$ is restricted to have a certain, relatively simple, form namely

$$\mathcal{F} = \{q|q = \prod_{i=1}^{N^2} q_i(\alpha_i) \prod_{\mu=1}^{M^2} q_\mu(\theta_\mu)\} \quad (\text{A-19})$$

With this form the problem in Eq. (A-18) can be efficiently solved with the VBEM algorithm [54]. The VBEM iterative updates the factors of the mean field approximation in Eq. (A-19). The update equations are given as

$$q(\theta_\mu) = \frac{1}{2\pi I_0\left(\frac{2}{\sigma_n^2}|y_\mu^* \langle z_\mu \rangle|\right)} \exp\left(\frac{2}{\sigma_n^2} \mathcal{R}(y_\mu^* z_\mu e^{j\theta_\mu})\right) \quad (\text{A-20})$$

$$q(\alpha_i) = \mathcal{CN}(m_i, \Sigma_i) \quad (\text{A-21})$$

where,

$$\Sigma_i = \frac{\sigma_n^2 \sigma_\alpha^2}{\sigma_n^2 + \sigma_\alpha^2 \boldsymbol{\gamma}_i^H \boldsymbol{\gamma}_i} \quad (\text{A-22})$$

$$m_i = \frac{\sigma_n^2 \sigma_\alpha^2}{\sigma_n^2 + \sigma_\alpha^2 \boldsymbol{\gamma}_i^H \boldsymbol{\gamma}_i} \mathbf{r}_i^H \boldsymbol{\gamma}_i \quad (\text{A-23})$$

$$\mathbf{r}_i = \bar{\mathbf{y}} - \sum_{k \neq i} m_k \boldsymbol{\gamma}_k \quad (\text{A-24})$$

with

$$\bar{\mathbf{y}} = y_\mu e^{j\arg(y_\mu^* z_\mu)} \frac{I_1(\frac{2}{\sigma_n^2} |y_\mu^* z_\mu|)}{I_0(\frac{2}{\sigma_n^2} |y_\mu^* z_\mu|)}, \forall \mu \quad (\text{A-25})$$

$$z_\mu = \sum_{i=1}^{N^2} m_i \gamma_{\mu i} \quad (\text{A-26})$$

Appendix B

Python Code

B-1 Decomposition into transverse modes

```
1 import numpy as np
2 import scipy as sci
3 import scipy.optimize
4 import scipy.special
5 import scipy.sparse
6 import scipy.signal
7 import time
8 import matplotlib.pyplot as plt
9
10 def pol2cart(rho,theta):
11     x = rho*np.cos(theta)
12     y = rho*np.sin(theta)
13     return x,y
14
15 def cart2pol(x,y):
16     rho = np.sqrt(x**2+y**2)
17     theta = np.arctan2(y,x)
18     return rho,theta
19
20 def findbopt(V,l):
21
22     dlta = 0.00001
23     b = np.arange(0,1,dlta)
24     zeros = scipy.special.jn_zeros(l, 100)
25     zeros = zeros=zeros[zeros < V]
26     bzeros = 1-(zeros/V)**2
27     right = V*np.sqrt(b)*sci.special.kv(l+1,V*np.sqrt(b))/sci.special.kv(
28         l,V*np.sqrt(b))
28     left = V*np.sqrt(1-b)*sci.special.jv(l+1,V*np.sqrt(1-b))/sci.special.
29         jv(l,V*np.sqrt(1-b))
```

```

29     d = left-right
30     s = 0
31     bopt = np.zeros(100)
32     L = np.zeros(100)-1
33     for i in range(0,len(d)-1):
34         if (d[i] == 0 or d[i]*d[i+1] < 0) and not np.isclose(bzeros,i*
35             dlta,atol=0.001).any():
36             bopt[s]=i*dlta
37             L[s] = 1
38             s += 1
39
40     bopt = bopt[bopt>0]
41     bopt = bopt[::-1]
42     L = L[L>-0.5]
43
44     return bopt,L
45
46 def singleLP(V,l,m,mode=1,a=1,clad=0.1,npix=512):
47
48     x = np.linspace(-(a+clad), (a+clad), npix)
49     X,Y = np.meshgrid(x,x)
50     RHO_core,PHI = cart2pol(X,Y)
51     RHO_core[RHO_core > a] = 0.0
52     RHO_clad,PHI = cart2pol(X,Y)
53     RHO_clad[RHO_clad <= a] = 0.0
54
55     bopt,L = findbopt(V,l)
56
57     if m > len(bopt):
58         print "This mode does not exist"
59         Psicos = np.zeros(PHI.shape)
60         Psisin = np.zeros(PHI.shape)
61     else:
62         bopt = bopt[m-1]
63         U = V*np.sqrt(1-bopt)
64         R1 = sci.special.jv(l,U*RHO_core/a)/sci.special.jv(l,U)
65         R2 = sci.special.kv(l,W*RHO_clad/a)/sci.special.kv(l,W)
66         R2[np.isnan(R2)] = 0.0
67         R = R1 + R2
68         Psicos = R*np.cos(l*PHI)
69         Psisin = R*np.sin(l*PHI)
70
71     if mode == 1:
72         Psi = Psicos
73     else:
74         Psi = Psisin
75
76     return Psi
77
78 def list(V,lmax):
79
80     bopt = 0

```

```

81     L = 0
82     for l in range(0,lmax):
83         boptnew,Lnew = findbopt(V,l)
84         bopt = np.append(bopt,boptnew)
85         L = np.append(L,Lnew)
86         bopt = bopt[1::]
87         L = L[1::]
88
89     return bopt,L
90
91 def even(bopt,L,mode,V,a=1,clad=0.1,npix=512):
92
93     x = np.linspace(-(a+clad), (a+clad), npix)
94     X,Y = np.meshgrid(x,x)
95     RHO_core,PHI = cart2pol(X,Y)
96     RHO_core[RHO_core >= a] = 0.0
97     RHO_clad,PHI = cart2pol(X,Y)
98     RHO_clad[RHO_clad < a] = 0.0
99
100    U = V*np.sqrt(1-bopt[mode])
101    W = V*np.sqrt(bopt[mode])
102    R1 = sci.special.jv(L[mode],U*RHO_core/a)/sci.special.jv(L[mode],U)
103    R2 = sci.special.kv(L[mode],W*RHO_clad/a)/sci.special.kv(L[mode],W)
104    R2[np.isnan(R2)] = 0.0
105    R = R1 + R2
106    Psicos = R*np.cos(L[mode]*PHI)
107    Psicos /= np.linalg.norm(Psicos, 'fro')
108
109    return Psicos
110
111 def odd(bopt,L,mode,V,a=1,clad=0.1,npix=512):
112
113     x = np.linspace(-(a+clad), (a+clad), npix)
114     X,Y = np.meshgrid(x,x)
115     RHO_core,PHI = cart2pol(X,Y)
116     RHO_core[RHO_core >= a] = 0.0
117     RHO_clad,PHI = cart2pol(X,Y)
118     RHO_clad[RHO_clad < a] = 0.0
119
120     U = V*np.sqrt(1-bopt[mode])
121     W = V*np.sqrt(bopt[mode])
122     R1 = sci.special.jv(L[mode],U*RHO_core/a)/sci.special.jv(L[mode],U)
123     R2 = sci.special.kv(L[mode],W*RHO_clad/a)/sci.special.kv(L[mode],W)
124     R2[np.isnan(R2)] = 0.0
125     R = R1 + R2
126     Psisin = R*np.sin(L[mode]*PHI)
127     if Psisin.all() == 0:
128         Psisin = np.zeros(Psisin.shape)
129     else:
130         Psisin /= np.linalg.norm(Psisin, 'fro')
131
132     return Psisin
133

```

```

134 def field2(bopt,L,coeff,V,a=1,clad=0.1,npix=512):
135
136     Psi = np.zeros((npix,npix),dtype=complex)
137     for i in range(0, len(bopt)):
138         Psicos = even(bopt,L,i,V,a,clad,npix)
139         Psisin = odd(bopt,L,i,V,a,clad,npix)
140         Psi += coeff[2*i]*Psicos + coeff[2*i+1]*Psisin
141
142     return Psi
143
144 def MatPur(Psi,bopt,L,V,N):
145
146     coeff_hat = np.zeros(2*len(bopt),dtype=complex)
147     residual = Psi
148     i = 0
149     idx = []
150     while np.sum(np.abs(residual)) > 0.1 and i <= N:
151         print i
152         co = 0.0
153         for n in range(0,2*len(bopt)):
154             if n not in idx:
155                 if n % 2 == 0:
156                     mode = even(bopt,L,n/2,V)
157                 else:
158                     mode = odd(bopt,L,n/2,V)
159
160                 inprod = np.sum(residual*mode.conj())
161
162                 if np.abs(inprod) > np.abs(co):
163                     co = inprod
164                     ci = n
165                     atom = mode
166
167                 coeff_hat[ci] = co
168                 idx.append(ci)
169                 residual -= co * atom
170             i += 1
171
172     return coeff_hat, residual
173
174 def fastMatPur(Psi,bopt,L,V,N):
175
176     coeff_hat = np.zeros(2*len(bopt),dtype=complex)
177     residual = Psi
178     i = 0
179     idx = []
180     while np.sum(np.abs(residual)) > 1 and i < N:
181         co = 0.0
182         corr = np.zeros(2*len(bopt),dtype=complex)
183         for n in range(0,2*len(bopt)):
184             if n not in idx:
185                 if n % 2 == 0:
186                     mode = even(bopt,L,n/2,V)

```

```

187         else:
188             mode = odd(bopt,L,n/2,V)
189
190             inprod = np.sum(residual*mode.conj())
191             corr[n] = inprod
192
193             if np.abs(inprod) > np.abs(co):
194                 co = inprod
195                 ci = n
196                 atom = mode
197
198             coeff_hat[ci] = co
199             idx.append(ci)
200             residual -= co * atom
201             i += 1
202             print i
203
204     # Continue with a subset of atoms with high correlation
205     corr[np.abs(corr/max(corr)) < 0.9] = 0.0
206     nn = np.nonzero(corr)
207     for ii in np.nditer(nn):
208         if ii not in idx:
209             if ii % 2 ==0:
210                 mode = even(bopt,L,ii/2,V)
211             else:
212                 mode = odd(bopt,L,ii/2,V)
213                 inprod = np.sum(residual*mode.conj())
214                 if np.abs(inprod) > np.abs(co):
215                     co = inprod
216                     ci = ii
217                     atom = mode
218                 coeff_hat[ci] = co
219                 idx.append(ci)
220                 residual -= co * atom
221                 i += 1
222                 print i
223
224     return coeff_hat, residual
225
226 def inprod(Psi,bopt,L,V,N):
227
228     coeff_hat = np.zeros(2*len(bopt),dtype=complex)
229     residual = Psi
230     for n in range(0,2*len(bopt)):
231         print n
232         if n % 2 == 0:
233             mode = even(bopt,L,n/2,V)
234         else:
235             mode = odd(bopt,L,n/2,V)
236
237         coeff_hat[n] = np.sum(residual*mode.conj())
238         residual -= coeff_hat[n] * mode
239

```

```

240     return coeff_hat, residual
241
242
243 ## -- Code -- ##
244
245 V = 8          # V-number
246 lmax = 5        # maximum number of l modes
247 k = 0.8         # amount of zeros 0<k<1
248
249 ## compute b-values
250 bopt, L = list(V, lmax)
251
252 ## generate random modal coefficients
253 coeff = np.random.normal(size=2*len(bopt)) + 1j*np.random.normal(size=2*
   len(bopt))
254 coeff /= np.linalg.norm(coeff,2)
255 ## compute corresponding field
256 N = np.size(np.nonzero(coeff))
257 F = field2(bopt,L,coeff,V)
258
259 ## -- Decompose field into modes -- ##
260 t1 = time.time()
261 coeff_hat, residual = inprod(F,bopt,L,V,N)
262 t = time.time() - t1
263 print 'time elapsed:',t
264 ## compute corresponding field
265 Psi_hat = field2(bopt,L,coeff_hat,V)
266 F = field2(bopt,L,coeff,V)
267
268 ## -- Plot Results -- ##
269 plt.subplot(131)
270 plt.imshow(np.abs(F))
271 plt.subplot(132)
272 plt.imshow(np.abs(Psi_hat))
273 plt.subplot(133)
274 plt.imshow(np.abs(residual))
275 plt.show()
276
277 for c in coeff:
278     plt.polar(np.angle(c),np.abs(c),marker='o')
279 for c in coeff_hat:
280     plt.polar(np.angle(c),np.abs(c),marker='*')
281 plt.show()

```

B-2 Multimode fibre simulation

```

1 import numpy as np
2 import scipy.fftpack
3 import time
4
5
6 def ft(a):
7     A = scipy.fftpack.fftshift(scipy.fftpack.fft2(scipy.fftpack.fftshift(
8         a)))
9     r = np.sum(np.abs(a)**2)/np.sum(np.abs(A)**2)
10    return r*A
11
12 def ift(a):
13     A = scipy.fftpack.ifftshift(scipy.fftpack.ifft2(scipy.fftpack.
14         ifftshift(a)))
15     r = np.sum(np.abs(a)**2)/np.sum(np.abs(A)**2)
16     return r*A
17
18 def ls(H,F):
19     M,N,N = H.shape
20     A = np.zeros((N,N), dtype='complex128')
21     B = np.zeros((N,N), dtype='complex128')
22     G = np.zeros((N,N), dtype='complex128')
23     for m in range(0,M):
24         A += H[m].conj() * F[m]
25         B += np.abs(H[m])**2
26     G[B!=0] = A[B!=0] / B[B!=0]
27     return G
28
29 def fibre_image(u1,NZ):
30     for i in range(0, NZ):
31         u1 = u1 * np.exp(1j * 2 * np.pi * fibre_profile[i] * LZ / lmbda /
32                           NZ )
33         u1 = prop(u1, LZ / NZ)
34
35     u1 = prop(u1,LZ/NZ)
36
37     return u1
38
39 def prop(u1,z):
40     if dx >= (lmbda * z / L):
41         fx = np.arange(-1/(2 * dx),1/(2 * dx),1.0)
42         fy = np.arange(-1/(2 * dx),1/(2 * dx),1.0)
43
44         FX,FY = np.meshgrid(fy,fx)
45
46         H = np.exp(-1j * np.pi * lmbda * z * (FX**2 + FY**2))
47         U1 = ft(u1)

```

```

48         U2 = H * U1
49         u2 = ift(U2)
50
51     else:
52         h = 1 / (1j * lmbda * z) * np.exp( 1j * k / (2 * z) * (PX**2 + PY
53                                         **2))
53         H = ft(h)
54         U1 = ft(u1)
55         U2 = H * U1
56         u2 = ift(U2)
57
58     return u2
59
60 ## -- Code from here -- ##
61
62 N = 512*2      ## Grid size
63 maxit = 20      ## Number of iterations
64 D = 20          ## Number of images
65
66 ## fibre parameters
67 NZ = 2          ## Propagation length
68 lmbda = 1.0     ## Wavelength(normalised)
69 L = 1.0          ## Support length(normalised)
70 LZ = 0.0002     ## Propagation step length
71 dx = L / N      ## Sample size
72 k = 2 * np.pi / lmbda ## Wave number
73
74 ## -- fibre specifications -- ##
75
76 ## Fibreprofile specifications
77 px = np.linspace(-1.0,1.0,N)
78 pz = np.linspace(-1.0,1.0,NZ)
79
80 PX,PY = np.meshgrid(px,px)
81 RHO = np.sqrt(PX**2 + PY**2)
82 THETA = np.arctan2(PY,PX)
83
84 ## Define the fibre
85 inner_diameter = 0.50
86 outer_diameter = 0.70
87 phase_error = 10000.0
88
89 pp = (np.ones((N,N)) * (RHO < inner_diameter)).astype('float')
90
91 ## Refractive index of the fibre
92 fibre_profile = np.zeros((NZ,N,N),dtype='float64')
93 fibre_profile[:,RHO > outer_diameter] = 1.00
94 fibre_profile[:,RHO < outer_diameter] = 1.40
95 fibre_profile[:,RHO < inner_diameter] = 1.45
96
97 ## Imperfections in the fibre
98 for i in range(0,NZ):

```

```

99      error = np.abs(ifft(np.random.randn(N,N)) * np.exp(- (PX**2 + PY
100          **2) / 1.0**2)))
101      error = error/error.max()
102      fibre_profile[i] = (fibre_profile[i] + phase_error * error)
103  ## -- Multiframe Deconvolution -- ##
104
105 ## Initialisation
106 y = np.zeros((D,N,N),dtype='complex')
107 x = np.zeros((D,N,N),dtype='complex')
108 X = np.zeros((D,N,N),dtype='complex')
109 y_hat = np.zeros((D,N,N),dtype=complex)
110 Y_HAT = np.zeros((D,N,N),dtype=complex)
111 O_HAT = np.random.randn(N,N) + 1j*np.random.randn(N,N)
112
113 ## Acquire D input-output image pairs
114 for d in range(0,D):
115     x[d] = pp * np.exp(1j*np.random.randn(N,N))
116     X[d] = fft(x[d])
117     y[d] = fibre_image(x[d],NZ)
118
119 ## Find O via deconvolution
120 for i in range(0,maxit):
121     for d in range(0,D):
122         y_hat[d] = np.abs(y[d]) * np.exp(1j*np.angle(ifft(O_HAT*X[d]))) # magnitude constraint
123         Y_HAT[d] = ifft(y_hat[d])
124     O_HAT = ls(X,Y_HAT)
125     O_HAT = np.exp(1j*np.angle(O_HAT)) # phase only constraint
126
127 ## -- Imaging -- ##
128
129 ## Define target intensity (TUDelft flame)
130 # img = pil.open('TUflame.png')
131 # img = np.array(img)
132 # img = img[:, :, 0]
133 # img = 1.0/(img+0.0001)
134 # img[img == np.min(img)] = 0.0
135 # img = downsample(downsampel(downsampel(img)))
136 # pad = (N-np.shape(img)[0])/2
137 # img = np.pad(img, ((pad, pad), (pad, pad)), 'edge')
138 # y_target = np.copy(img)
139 # Y_TARGET = fft(y_target)
140
141 ## Define target intensity (spot)
142 y_target = np.zeros((N,N))
143 y_target[N/2, N/2] = 1.0
144 Y_TARGET = fft(y_target)
145
146 ## Compute input/output (PSF model)
147 Y_OUT_HAT = np.copy(Y_TARGET)
148 x_target_hat = pp * ifft(Y_OUT_HAT/O_HAT)
149 X_TARGET_HAT = fft(pp * np.exp(1j*np.angle(x_target_hat)))

```

```

150 y_out_hat = ift(O_HAT*X_TARGET_HAT)
151 y_out_hat /= np.sum(np.abs(y_out_hat)**2)
152
153 ## Compute input/output (Fibre simulation)
154 X_TARGET = Y_TARGET/O_HAT
155 x_target = pp * np.exp(1j*np.angle(ift(X_TARGET)))
156 y_out = fibre_image(x_target,NZ)
157 y_out /= np.sum(np.abs(y_out)**2)
158 Y_OUT = ft(np.abs(y_out))
159
160
161 ## -- Plot results -- ##
162
163 phi = np.zeros((N,N))
164 rad = pp * (np.angle(x_target)+np.pi)/(2.0*np.pi)
165 phi[255,255:769] = 1.0
166 phi[769,255:769] = 1.0
167 phi[255:769,255] = 1.0
168 phi[255:769,769] = 1.0
169 phi += rad
170 phi = phi[254:N-254,254:N-254]
171
172 images = [np.abs(y_out_hat[254:N-254,254:N-254])**2,np.abs(y_out[254:N-254,254:N-254])**2,phi]
173 title = ['Model intensity','Fibre simulator intensity','SLM phase pattern (rad)']
174 i=0
175 fig, axes = plt.subplots(nrows=1, ncols=3, figsize=(9.75, 3))
176 for ax in axes.flat:
177     im = ax.imshow(images[i],cmap='Blues')
178     a = plt.axes([.2, .3, .15, .15])
179     a.imshow(np.abs(y_out_hat[254+225:N-254-225,254+225:N-254-225])**2,
180             cmap='Blues')
181     plt.setp(a, xticks=[], yticks[])
182     a = plt.axes([.42, .3, .15, .15])
183     a.imshow(np.abs(y_out[254+225:N-254-225,254+225:N-254-225])**2,cmap='Blues')
184     plt.setp(a, xticks=[], yticks[])
185     ax.set_title(title[i])
186     i+=1
187
188 cbar = fig.colorbar(im, ax=axes.ravel().tolist(), shrink=0.45, ticks=[0,0.5,1])
189 cbar.ax.set_yticklabels(['0', '$\pi$', '2$\pi$'])
190 plt.show()

```

Bibliography

- [1] A. Mosk, A. Lagendijk, G. Leroey, and M. Fink, “Controlling waves in space and time for imaging and focusing in complex media,” *Nature Photonics*, vol. 6, pp. 283–292, 2012.
- [2] I. Vellekoop and A. Mosk, “Phase control algorithms for focusing light through turbid media,” *Optics Communications*, vol. 281, no. 11, pp. 3071–3080, 2008.
- [3] G. Keiser, *Optical Fiber Communications*. McGraw-Hill Education, 2010.
- [4] I. Vellekoop and A. Mosk, “Focusing coherent light through opaque strongly scattering media,” *Optics Letters*, vol. 32, no. 16, pp. 2309–2311, 2007.
- [5] J. Aulbach, B. Gjonaj, P. M. Johnson, A. P. Mosk, and A. Lagendijk, “Control of light transmission through opaque scattering media in space and time,” *Physical review letters*, vol. 106, no. 10, p. 103901, 2011.
- [6] B. Coyotl-Ocelotl, R. Porras-Aguilar, R. Ramos-Garcia, and J. Ramirez-San-Juan, “Implementation of focusing and redirecting light through highly scattering media,” in *SPECKLE 2015: VI International Conference on Speckle Metrology*, pp. 96601X–96601X, International Society for Optics and Photonics, 2015.
- [7] R. Horstmeyer, H. Ruan, and C. Yang, “Guidestar-assisted wavefront-shaping methods for focusing light into biological tissue,” *Nature Photonics*, vol. 9, no. 9, pp. 563–571, 2015.
- [8] I. Vellekoop, E. Van Putten, A. Lagendijk, and A. Mosk, “Demixing light paths inside disordered metamaterials,” *Optics express*, vol. 16, no. 1, pp. 67–80, 2008.
- [9] M. Kim, Y. Choi, C. Yoon, W. Choi, J. Kim, Q.-H. Park, and W. Choi, “Maximal energy transport through disordered media with the implementation of transmission eigenchannels,” *Nature photonics*, vol. 6, no. 9, pp. 581–585, 2012.
- [10] I. Vellekoop and A. Mosk, “Universal optimal transmission of light through disordered materials,” *Physical Review Letters*, vol. 101, no. 12, pp. 120601–1–120601–4, 2008.

- [11] H. A. Haus, “Waves and fields in optoelectronics (prentice-hall series in solid state physical electronics),” 1984.
- [12] P. Sheng, *Introduction to wave scattering, localization and mesoscopic phenomena*, vol. 88. Springer Science & Business Media, 2006.
- [13] R. N. Mahalati, D. Askarov, J. P. Wilde, and J. M. Kahn, “Adaptive control of input field to achieve desired output intensity profile in multimode fiber with random mode coupling,” *Optics express*, vol. 20, no. 13, pp. 14321–14337, 2012.
- [14] Y. Imry, “Active transmission channels and universal conductance fluctuations,” *EPL (Europhysics Letters)*, vol. 1, no. 5, p. 249, 1986.
- [15] S. Popoff, G. Lerosey, R. Caminati, M. Fink, A. Boccara, and S. Gigan, “Measuring the transmission matrix in optics: an approach to the study and control of light propagation in disordered media,” *Physical Review Letters*, vol. 104, no. 10, pp. 100601–1–100601–4, 2010.
- [16] S. Popoff, G. Lerosey, M. Fink, A. C. Boccara, and S. Gigan, “Image transmission through an opaque material,” *Nature Communications*, vol. 1, p. 81, 2010.
- [17] S. Bianchi and R. Di Leonardo, “A multi-mode fiber probe for holographic micromanipulation and microscopy,” *Lab on a Chip*, vol. 12, no. 3, pp. 635–639, 2012.
- [18] D. Loterie, S. Farahi, I. Papadopoulos, A. Goy, D. Psaltis, and C. Moser, “Digital confocal microscopy through a multimode fiber,” *Optics express*, vol. 23, no. 18, pp. 23845–23858, 2015.
- [19] M. Plöschner, V. Kollárová, Z. Dostál, J. Nylk, T. Barton-Owen, D. E. Ferrier, R. Chmelík, K. Dholakia, and T. Čižmár, “Multimode fibre: Light-sheet microscopy at the tip of a needle,” *Scientific reports*, vol. 5, 2015.
- [20] T. Čižmár and K. Dholakia, “Shaping the light transmission through a multimode optical fibre: complex transformation analysis and applications in biophotonics,” *Optics Express*, vol. 19, no. 20, pp. 18871–18884, 2011.
- [21] A. Liutkus, D. Martina, S. Popoff, G. Chardon, O. Katz, G. Lerosey, S. Gigan, L. Daudet, and I. Carron, “Imaging with nature: Compressive imaging using a multiply scattering medium,” *Scientific reports*, vol. 4, 2014.
- [22] R. W. Gerchberg, “A practical algorithm for the determination of phase from image and diffraction plane pictures,” *Optik*, vol. 35, p. 237, 1972.
- [23] M. L. Moravec, J. K. Romberg, and R. G. Baraniuk, “Compressive phase retrieval,” in *Optical Engineering+ Applications*, pp. 670120–670120, International Society for Optics and Photonics, 2007.
- [24] P. Schniter and S. Rangan, “Compressive phase retrieval via generalized approximate message passing,” *IEEE Transactions on Signal Processing*, vol. 63, no. 4, pp. 1043–1055, 2015.

- [25] Y. Shechtman, A. Beck, and Y. C. Eldar, “Gespar: Efficient phase retrieval of sparse signals,” *IEEE transactions on signal processing*, vol. 62, no. 4, pp. 928–938, 2014.
- [26] H. Yilmaz, W. Vos, and A. Mosk, “Optimal control of light propagation through multiple-scattering media in the presence of noise,” *Biomedical Optics Express*, vol. 4, no. 9, pp. 1759–1768, 2013.
- [27] A. Drémeau, A. Liutkus, D. Martina, O. Katz, C. Schülke, F. Krzakala, S. Gigan, and L. Daudet, “Reference-less measurement of the transmission matrix of a highly scattering material using a dmd and phase retrieval techniques,” *Optics Express*, vol. 23, no. 9, pp. 11898–11911, 2015.
- [28] R. Brüning, D. Flamm, S. S. Ngcobo, A. Forbes, and M. Duparré, “Rapid measurement of the fiber’s transmission matrix,” in *SPIE OPTO*, pp. 93890N–93890N, International Society for Optics and Photonics, 2015.
- [29] R. Y. Gu, R. N. Mahalati, and J. M. Kahn, “Design of flexible multi-mode fiber endoscope,” *Optics express*, vol. 23, no. 21, pp. 26905–26918, 2015.
- [30] M. Plöschner, T. Tyc, and T. Čižmár, “Seeing through chaos in multimode fibres,” *Nature Photonics*, vol. 9, no. 8, pp. 529–535, 2015.
- [31] J. Carpenter, B. J. Eggleton, and J. Schröder, “110x110 optical mode transfer matrix inversion,” *Optics express*, vol. 22, no. 1, pp. 96–101, 2014.
- [32] Y. Choi, C. Yoon, M. Kim, T. D. Yang, C. Fang-Yen, R. R. Dasari, K. J. Lee, and W. Choi, “Scanner-free and wide-field endoscopic imaging by using a single multimode optical fiber,” *Physical review letters*, vol. 109, no. 20, p. 203901, 2012.
- [33] A. A. Boechat, D. Su, D. R. Hall, and J. D. Jones, “Bend loss in large core multimode optical fiber beam delivery systems,” *Applied optics*, vol. 30, no. 3, pp. 321–327, 1991.
- [34] B. E. Saleh, M. C. Teich, and B. E. Saleh, *Fundamentals of photonics*, vol. 22. Wiley New York, 1991.
- [35] E. J. Candes, Y. C. Eldar, T. Strohmer, and V. Voroninski, “Phase retrieval via matrix completion,” *SIAM review*, vol. 57, no. 2, pp. 225–251, 2015.
- [36] E. J. Candes, T. Strohmer, and V. Voroninski, “Phaselift: Exact and stable signal recovery from magnitude measurements via convex programming,” *Communications on Pure and Applied Mathematics*, vol. 66, no. 8, pp. 1241–1274, 2013.
- [37] I. Waldspurger, A. d’Aspremont, and S. Mallat, “Phase recovery, maxcut and complex semidefinite programming,” *Mathematical Programming*, vol. 149, no. 1-2, pp. 47–81, 2015.
- [38] A. Dremeau and F. Krzakala, “Phase recovery from a bayesian point of view: the variational approach,” in *2015 Acoustics, Speech and Signal Processing, IEEE International Conference*, pp. 3661–3665, IEEE, 2015.
- [39] E. Osherovich, “Numerical methods for phase retrieval,” *arXiv preprint arXiv:1203.4756*, 2012.

- [40] J. R. Fienup, "Reconstruction of an object from the modulus of its fourier transform," *Optics letters*, vol. 3, no. 1, pp. 27–29, 1978.
- [41] M. X. Goemans and D. P. Williamson, "Improved approximation algorithms for maximum cut and satisfiability problems using semidefinite programming," *Journal of the ACM (JACM)*, vol. 42, no. 6, pp. 1115–1145, 1995.
- [42] S. Rangan, "Generalized approximate message passing for estimation with random linear mixing," in *Information Theory Proceedings (ISIT), 2011 IEEE International Symposium on*, pp. 2168–2172, IEEE, 2011.
- [43] A. Demeau, "prVBEM implementation author's webpage." http://angelique.demeau.free.fr/Site_anglais/Publications.html. Accessed: 2016-02-02.
- [44] A. d. Fajwel Fogel, Irène Waldspurger, "PhaseCut implementation author's webpage." <http://www.di.ens.fr/data/software/>. Accessed: 2016-05-02.
- [45] C. Helmberg, F. Rendl, R. J. Vanderbei, and H. Wolkowicz, "An interior-point method for semidefinite programming," *SIAM Journal on Optimization*, vol. 6, no. 2, pp. 342–361, 1996.
- [46] R. A. Gonsalves, "Phase retrieval and diversity in adaptive optics," *Optical Engineering*, vol. 21, no. 5, pp. 215829–215829, 1982.
- [47] R. Paxman, T. Schultz, and J. Fienup, "Joint estimation of object and aberrations by using phase diversity," *Journal of the Optical Society of America A*, vol. 9, no. 7, pp. 1072–1085, 1992.
- [48] J. W. Goodman, *Introduction to Fourier optics*. Roberts and Company Publishers, 2005.
- [49] A. M. Caravaca-Aguirre, E. Niv, D. B. Conkey, and R. Piestun, "Real-time resilient focusing through a bending multimode fiber," *Optics express*, vol. 21, no. 10, pp. 12881–12887, 2013.
- [50] M. Plöschner, B. Straka, K. Dholakia, and T. Čižmár, "Gpu accelerated toolbox for real-time beam-shaping in multimode fibres," *Optics express*, vol. 22, no. 3, pp. 2933–2947, 2014.
- [51] S. Farahi, D. Ziegler, I. N. Papadopoulos, D. Psaltis, and C. Moser, "Dynamic bending compensation while focusing through a multimode fiber," *Optics express*, vol. 21, no. 19, pp. 22504–22514, 2013.
- [52] D. Conkey, A. Caravaca-Aguirre, and R. Piestun, "High-speed phase-control of wavefronts with binary amplitude dmd for light control through dynamic turbid media," in *Proceeding SPIE, MEMS Adaptive Optics VII*, p. 8617, SPIE, 2015.
- [53] M. Volckaert, "Nonlinear iterative learning control through dynamic optimization (niet lineaire iteratief lerende regeling door dynamische optimalisatie)," 2012.
- [54] J. Bernardo, M. Bayarri, J. Berger, A. Dawid, D. Heckerman, A. Smith, M. West, *et al.*, "The variational bayesian em algorithm for incomplete data: with application to scoring graphical model structures," *Bayesian statistics*, vol. 7, pp. 453–464, 2003.

Glossary

List of Acronyms

NA	Numerical Aperture
PSF	Point Spread Function
MMF	Multi Mode Fibre
SLM	Spatial Light Modulator
TM	Transmission Matrix
DMD	Digital Micromirror Device
ILC	Iterative Learning Control
OTF	Optical Transfer Function
DFT	Discrete Fourier Transform

